NASA Technical Memorandum 104586

Convective and Stratiform Rain: Multichannel Microwave Sensing Over Oceans

C. Prabhakara, J. J. Nucciarone,
and G. Dalu

June 1993

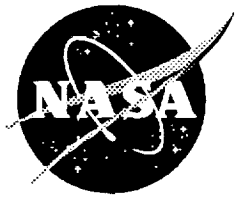

NASA Technical Memorandum 104586

Convective and Stratiform Rain: Multichannel Microwave Sensing Over Oceans

C. Prabhakara
NASA Goddard Space Flight Center
Greenbelt, Maryland

J. J. Nucciarone
Hughes STX Corporation
Lanham, Maryland

G. Dalu
C.N.R.
Area Della Receria Di Cagliari, Italy

National Aeronautics and
Space Administration

Goddard Space Flight Center
Greenbelt, Maryland 20771

1993

Convective and Stratiform Rain: Multichannel Microwave Sensing Over Oceans

Measurements made by the Special Sensor Microwave/Imager (SSM/I) radiometer over the oceans, at 19, 37, and 85 GHz in dual polarization, are used to develop a model to classify rain into light-stratiform, moderately convective, and heavy convective types in the mesoscale convective systems (MCS). It is observed that the bulk of the 19- and 37-GHz data are linearly correlated with respect to one another, and generally increase together in brightness as the mean rain rate in the field of view (*fov*) of the radiometer increases. However, a significant fraction of the data from these channels departs from this linear relationship reflecting the non-uniform rain that is convective vs. the relatively light stratiform rain. It is inferred from the SSM/I data, in a MCS, that when the slope dT_{37}/dT_{19} is greater than unity there are optically thin clouds that produce light uniform rain. On the other hand, when dT_{37}/dT_{19} is close to unity the rain cells have an open structure and correspond to the convective type of rain. The openings between the cells are apparently a result of the downdrafts and/or entrainment. Relatively low values of 85-GHz brightness temperatures that are present when dT_{37}/dT_{19} is close to unity support these views and, in addition, leads us to conclude that when the convection is heavy this brightness temperature decreases due to scattering by hydrometeors. On the basis of this explanation of the SSM/I data, an empirical rain retrieval algorithm is developed. Radar backscatter observations over the Atlantic Ocean next to Florida are used to demonstrate the applicability of this method. Three monthly mean maps of rainfall over the oceans, from 50° N to 50° S, are presented to illustrate the ability of this method to sense seasonal and interannual variations of rain.

Introduction

Rainfall over oceans is an important element of the hydrological cycle. Satellite remote sensing of rain, proposed in projects such as TRMM (Simpson, 1988), should improve our knowledge about seasonal and interannual variation of rain and enable us to comprehend the mechanisms leading to global climate change.

Multichannel microwave radiometers SMMR (Gloersen and Hardis, 1978) and SSM/I (Hollinger *et al.*, 1987) flown on the Nimbus 7 and DMSP satellites can contribute significantly to the progress on remote sensing of rain over oceans. Commonly, the frequency-dependent extinction characteristics of these multichannel radiometers are assumed to help one to measure rain intensity and to discriminate among rain, cloud liquid (see e.g., Wilheit *et al.*, 1982; Wu and Weinman, 1984), and ice phase of the hydrometeors. However, the following reasons lead to considerable difficulties in relating the radiometer measurements to the hydrometeors: 1) the SMMR and SSM/I radiometers have a field of view (*fov*)[1] that is large, about 30 km (at 37 GHz), compared to the size of the rain cells, which are on the order of a few km. This is an important factor because the rain rate from such cells can be very non-uniformly distributed in the *fov*; 2) theoretical simulations (See e.g., Olson, 1987), neglecting ice scattering, show that at microwave frequencies below about 37 GHz as the rain rate increases, the brightness temperature measured by the radiometer shows an initial linear increase and then asymptotically reaches a maximum value of approximately 265 K. The radiometer loses sensitivity beyond that point. This maximum value, which is close to the freezing point, is descriptively referred to as the saturation brightness temperature. For example, at 37 GHz, the radiometer reaches the saturation temperature and loses sensitivity beyond a threshold of about 4 mm/h rain rate. Hence, measurements made by the radiometer are reflecting the combined effect of areas in the *fov* constituted by a) clear ocean, b) cloud liquid water and light rain, which have a brightness temperature below the saturation temperature; and more importantly c) the rain area in the *fov* that has a saturation brightness temperature. Therefore, in order to retrieve *fov*-averaged rain rates over oceans it is necessary to have information about the distribution of these elements in the *fov*—preferably from the radiometer data. This study is an attempt to gather this information.

---

[1]The *fov* of various channels of the radiometers on SMMR and SSM/I depends inversely on the microwave frequency of the channel.

Inference of Spatial Distribution

A background knowledge of the extinction properties of the hydrometeors at the SSM/I frequencies 19- , 37- , and 85-GHz, is very helpful for the following discussion. These extinction properties are illustrated in Fig. 1. At all these frequencies, raindrop absorption is much stronger than that of ice particles. In addition, this absorption increases both with the frequency of microwave radiation and with the rain rate. Thus the thermal emission of the hydrometeors at all frequencies will be mainly from water particles. Ice particles, on the other hand, can make a significant contribution to the scattering of microwave radiation. At 85.5 GHz, ice scattering exceeds that of water drop scattering. According to Fig. 1 for rain rates under 20 mm/h the ice scattering coefficient at 85.5 GHz is an order of magnitude larger than that at 37 GHz. These absorption and scattering properties are important factors that govern the radiative transfer in the microwave region.

In an earlier study, Prabhakara *et al.*, 1992 (hereafter referred to as PDNSL) showed from SMMR and SSM/I observations that the data up to the frequency, ν, of 37 GHz over oceans are highly correlated and essentially give us a measure of the effective rain area when we neglect the weak scattering effect. At a given frequency ($\nu < 37$ GHz), this effective rain area represents the area in the *fov* of the radiometer that has a rain rate above a certain threshold and hence has the saturation brightness temperature. Thus when the entire *fov* has a rain rate above that threshold the radiometer senses the saturation brightness temperature. This inference was supported by the polarization effect. One expects over oceans, where the sea surface essentially polarizes the microwave radiation, the polarization difference, pd, (i.e. the brightness temperature difference between the vertically and horizontally polarized components of the radiation) depends on the sea surface area in the radiometer *fov* that is not masked by dense clouds and rain. As a result, over the oceans, pd is inversely proportional to the brightness temperature. Hence, the pd is redundant and does not contain information that is independent of the brightness temperature. PDLNS showed that this is true up to the 37-GHz frequency, where there is apparent weak scattering of microwave radiation by hydrometeors. When the scattering effect is strong, as at 85 GHz, this inverse relationship breaks down.

The study of PDNSL also contained radiative transfer theoretical calculations, based on the model of Kummerow *et al.* (1989), to simulate the SSM/I observations. It was inferred that since the aereal distribution of the hydrometeors could not be prescribed adequately in such calculations, the

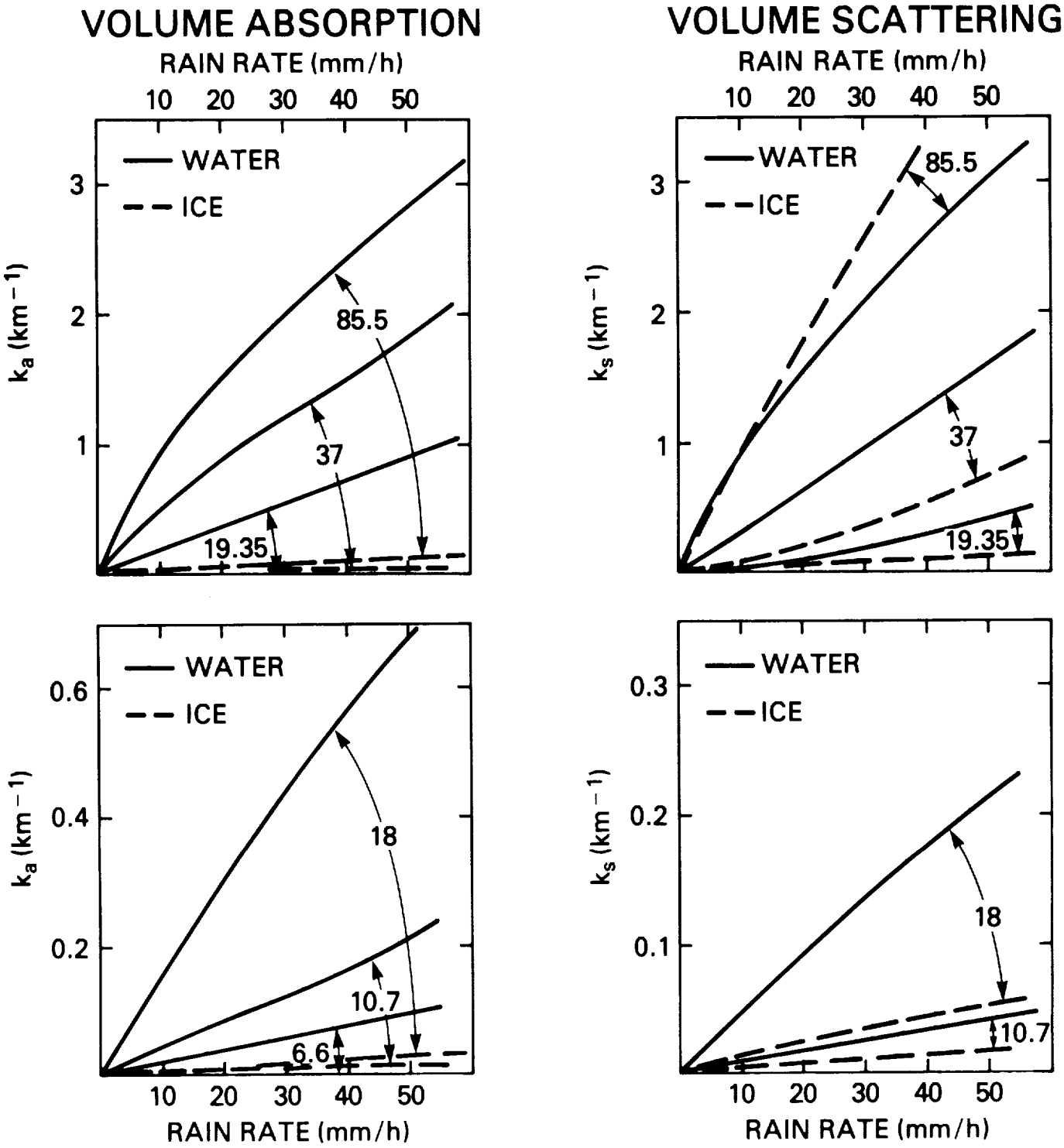

Fig. 1: Volume absorption and scattering coefficients, k_a (km^{-1}) and k_s (km^{-1}) in the microwave region between 6.6 and 85 GHz (based on: Olson, 1987, Spencer *et al.*, 1989).

correlation between various channels as stated above could not be simulated satisfactorily. However, the inverse correlation between the brightness temperature and *pd* at a given frequency could be simulated when the scattering was negligible. Because of scattering effects, SSM/I measurements at the higher frequencies, e.g., 85 GHz, do not correlate well with the measurements at the lower frequencies. PDLNS therefore inferred that this high-frequency channel gives independent information pertaining mainly to hydrometeors above rain clouds. However, this independent information was not exploited by PDLNS because the interrelationship between observations at this high frequency and that at low frequencies was not fully understood. In order to assess this interrelationship, we are presenting graphical analysis of data at 19, 37, and 85 GHz in Fig. 2a and 2b.

Fig. 2a shows a bi-directional histogram (**bdh**) of SSM/I brightness temperature data at the 19- and 37-GHz channels, i.e., T_{19} and T_{37}, composited from 1 month of observations in a limited oceanic region of 3° latitude by 5° longitude. The limited spatial and temporal span of the data is expected to minimize the variance due to changes in time and space. In this figure, the 19- and 37-GHz data are grouped into 5 K by 5 K brightness temperature bins and the number of data points that fall into each bin is shown. One notices from the figure along the ordinate in a particular 5 K interval of T_{37}, the T_{19} can have a significant range of values. For example, in one T_{37} interval, 210° - 215°, the T_{19} varies over 5 intervals, from 155 to 180 K. Similarly, for a particular interval of T_{19}, the T_{37} can vary over an appreciable range. One can also notice that there is a tendency for a maximum number of observations to lie along the middle of the **bdh** as depicted in the figure. These characteristics of the **bdh** require explanation.

The sensitivity of T_{19} and T_{37} to the commonly known parameters (see e.g., Prabhakara *et al.*, 1983; Wilheit, 1978), i.e. sea surface temperature, columnar water vapor content in the atmosphere, surface wind speed, and rain rate cannot fully explain the character of the **bdh**. We need a new physical process to explain this character. The mean brightness temperature T_{85} in each one of the 5 K by 5 K bins as determined from SSM/I 85-GHz measurements, helps us to unravel this physical process. The 85-GHz channel has the smallest *fov*, ~15 km, and compared to the lower frequency channels has a very large scattering coefficient due to ice and water particles.

We find from Fig. 2b that to the right side of the maximum in the **bdh** , there are some T_{85} data that have values well below 240 K. These data are

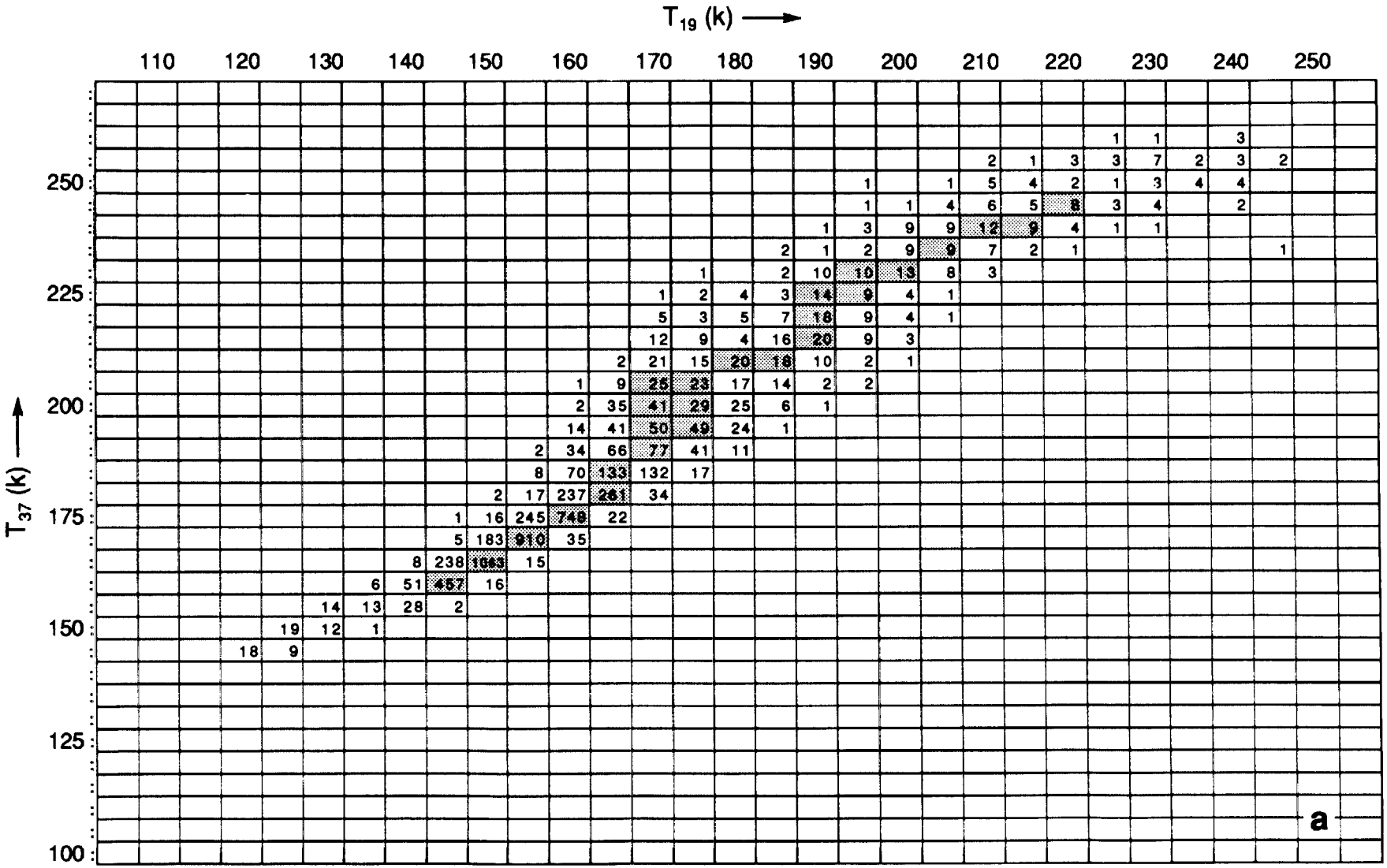

Fig. 2: a) Bi-directional histogram of the SSM/I 19- and 37-GHz brightness temperature data for the month of June, 1989, in the oceanic region 22° - 25° N Latitude and 130° - 135° E longitude. The frequency of the data is sorted into 5 K by 5 K brightness temperature bins. The bins with the maximum observed frequency are shaded.

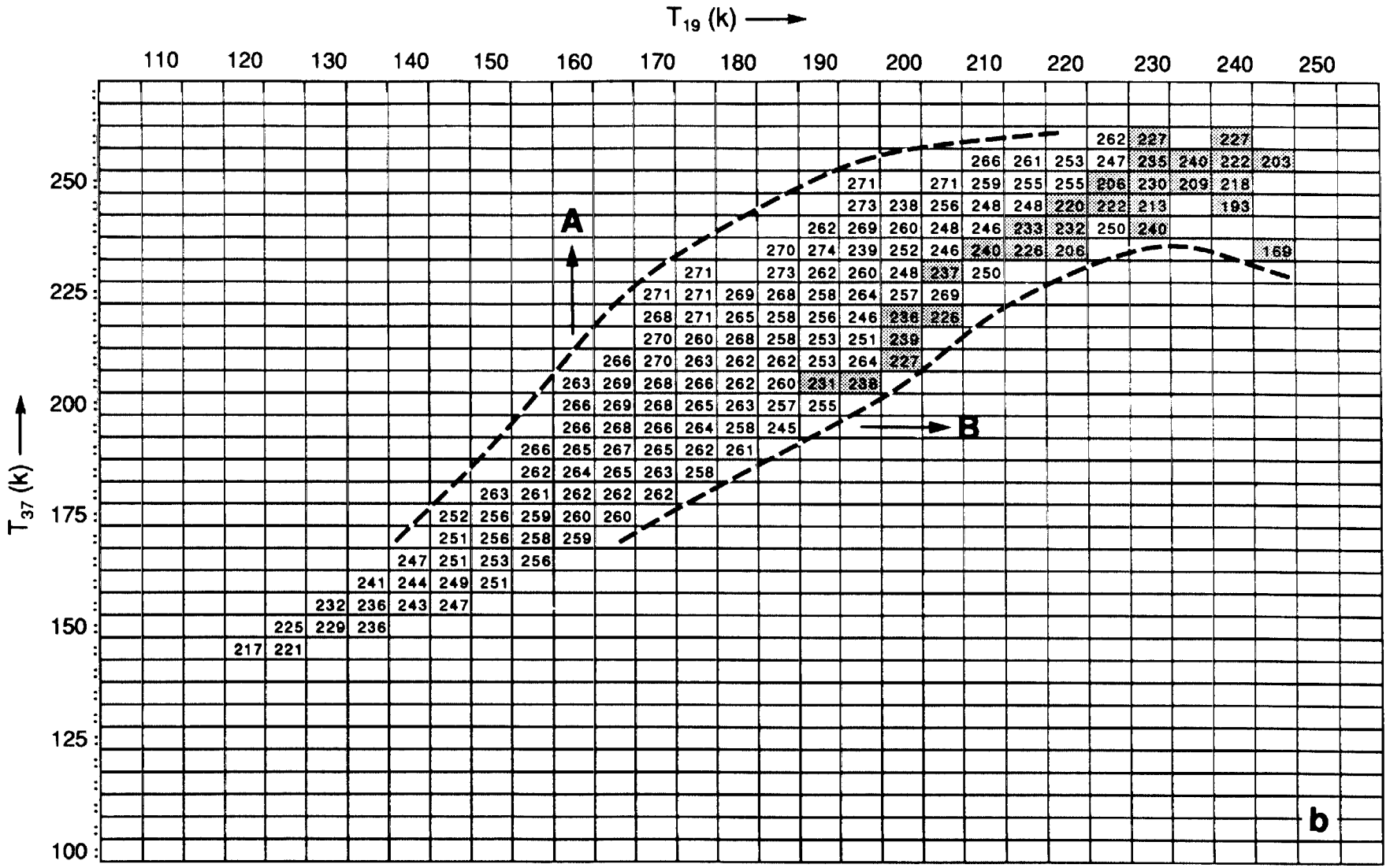

b) Mean 85-GHz brightness temperature T_{85} K corresponding to the bins shown in Fig. 2a. Values of T_{85} less than 240 K are shaded. The data between the heavy dashed line **A** and the locus of the frequency maximum tend to indicate extensive cloudiness and light rain. The data between the locus of the frequency maximum and the heavy dashed line **B** tend to indicate broken cumulus clouds and moderate convective rain. Shaded bins with T_{85} < 240 K indicate scattering by hydrometeors generated in severe convective clouds.

displayed in Fig. 2b with shading. Along the opposite side most of the T_{85} observations are close to or larger than 260 K. The scattering of the 85-GHz radiation by hydrometeors, that are present on top of intense convective systems, decreases T_{85} to values well below 240 K. Hence the presence of these data along one side of the **bdh** suggests a preferential combination of T_{19}, T_{37}, and T_{85} that pertain to strong convection. Apparently along the left side of the **bdh** heavy rain events are not probable.

Based on the above analysis we are able to identify three rain regimes in the **bdh**. Two regimes identified with heavy dashed lines in Fig. 2b are differentiated with the help of the slope (dT_{37}/dT_{19}). This slope is greater than unity for the dashed line to the left side of the **bdh** and close to unity for the other. Based on the sensitivity of T_{37} and T_{19} to the hydrometeors we infer the regime with slope greater than unity has extensive cloudiness with very light rain. The other regime corresponds to moderate convective rain clouds that are broken. Apparently, the broken clouds are a consequence of entrainment and downdrafts that compensate for the updrafts. In addition to the above two regimes, we infer that the T_{85} observations that are well below 240 K in the **bdh** where $dT_{37}/dT_{19} \sim 1$ indicate the presence of severe convective rain. This third regime is superimposed on the moderate convection.

The explanation given above for the three regimes is further clarified with the help of schematic figures Fig. 3a, b, and c. The *fov* of the radiometer, depicted in these figures, shows different oceanic scenes. In one, Fig. 3a, there is an extensive cloud system that is not opaque to the microwave radiation, while in the second, Fig. 3b, there are thick broken rain clouds. The brightness temperature observed by the satellite-borne radiometer in these two scenes is influenced quite differently by the sea surface and clouds. In the case corresponding to Fig. 3a, the transmission and emission of the clouds that are spectrally dependent are important in determining the brightness temperature. On the other hand, the fractional areas constituted by open water and moderately thick rain clouds that are dissipating due to entrainment and downdrafts essentially control the brightness temperature in Fig. 3b. It is conceivable that there can be two ocean scenes that belong to these two regimes, such that at 37 GHz, the brightness temperatures are nearly equal. However at 19 GHz, having different extinction properties, the brightness temperature corresponding to two such scenes will not be the same. T_{19} in case (a) will be smaller compared to that in case (b). The third regime is depicted in Fig. 3c. Some tall cumulonimbus clouds with ice anvils on top distinguish this regime from the moderately convective type that is shown in Fig. 3b.

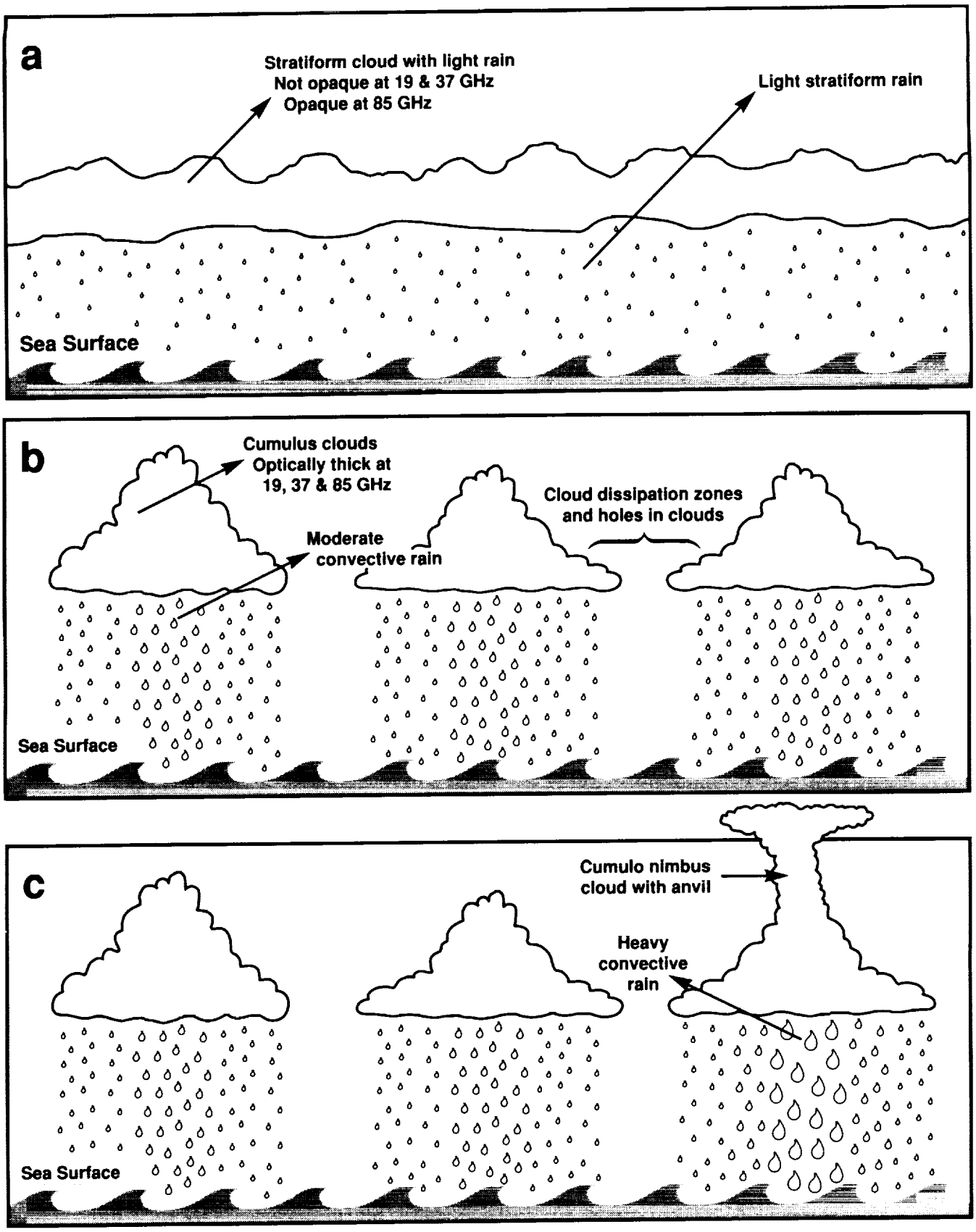

Fig. 3: Schematic picture showing the nature of clouds, over the ocean background, in the radiometer field of view.

a) Thin stratiform cloud sheets with light rain.

b) Convective clouds with dissipation zone and holes. The presence of moderate convective rain is shown.

c) Isolated cumulus nimbus clouds with intense rain along with regular cumulus clouds and rain.

The frequency maximum along the middle of the **bdh** suggests that most of the data represent a various mix of the two limiting cases; namely, thin and thick clouds filling the *fov*.

The physical mechanisms that lead to the three cases shown in Figs. 3 a, b, and c are all part of convection that has a complex highly non-linear nature. Here the SSM/I data corresponding to these cases are empirically designated to represent light-stratiform, moderately convective, and heavy convective rain types. When carefully calibrated radar ground-truth information about rain is available, it will be possible to classify SSM/I rain data more thoroughly.

Multichannel Empirical Model to Estimate Rain Rate Over Oceans

Based on our examination (see also PDNLS) of the SSM/I multichannel dual polarization data, which takes into consideration the extinction properties in these channels, we find there are four independent pieces of information in these microwave data that can be useful in the remote sensing of rain:

1) The microwave radiometer measurements in dual polarization up to a frequency of about 37 GHz strongly relate to the area, in the radiometer *fov*, that has a rain rate in excess of a threshold. This is called the effective rain area.

2) The data at two frequencies, below about 37 GHz, can be useful in discriminating, in a relative manner, the uniform light vs. non-uniform moderately convective nature of the rain in the *fov* of the radiometer. This is discussed in the previous section with the help of SSM/I 19- and 37-GHz data. These channels have extinction values that are sufficiently differentiated and are well suited for this purpose of discrimination.

3) The 85-GHz data contain independent information that relates to ice scattering that can be useful to highlight heavy convective rain.

4) Total water-vapor content in a column of the atmosphere can be sensed from microwave measurements near the 22.235-GHz weak water-vapor line. This total water-vapor amount depends on the sea surface temperature and the thermal structure in the lower troposphere (Prabhakara *et al.*, 1977). Further, the liquid water content of the clouds depends on the thermal conditions (Feigelson, 1978). From these interrelationships we assume the cloud liquid-water content, and hence rain, is dependent on the total water-vapor content of the atmosphere. Thus this parameter—total water vapor—can be useful for global mapping of rain.

These four parameters mentioned above do not relate in a simple fashion to the mean rain rate in the radiometer *fov*. Further, because of the highly non-uniform distribution in the radiometer *fov* of the rain, liquid water in the clouds, and ice particles of different kinds, these hydrometeors cannot be distinguished by their spectral signatures. So one takes an empirical approach to sense rain rate. Examples of such empirical models are Prabhakara *et al.*, 1986, Shin *et al.*, 1990, and Wilheit *et al.*, 1991.

It is also possible to simulate rainfall numerically with convective cloud models (e.g., Smith and Mugnai, 1992; Tao *et al.*, 1991; Adler *et al.*, 1991). With the help of numerically simulated distributions of hydrometeors one can calculate, using radiative transfer theory, the upwelling brightness temperatures at different microwave frequencies corresponding to those of SMMR or SSM/I. One can then draw relationships between the numerically simulated rain rates and the microwave brightness temperatures. Such relationships could then be applied to the satellite microwave radiometer data to estimate rain rate assuming that the numerical models can satisfactorily represent nature.

We have adopted a different approach to this problem. First the information content of the satellite data is explored and then that information is applied to an empirical rain retrieval model. The empirical model to retrieve rain rates from SMMR and SSM/I data developed by PDNSL based on the total water vapor content in the atmosphere and the effective rain area is along such lines. The aim of this study is to improve the model of PDNSL with the additional information conveyed by the 85-GHz data and the slope (dT_{37}/dT_{19}).

Based on the hypothesis that at one instance over a given oceanic region the probability distribution function (pdf) of log R and the pdf of the brightness temperatures at 37 GHz, are related the following equation, involving two parameters, was deduced empirically by PDNSL to estimate rain rate, R.

$$R = \exp [\beta(w)(T_{37} - T_{37}^*)]^{\gamma} - 1 \qquad [1]$$

The two parameters in eq.(1) are $\beta(w)$, which depend on the water-vapor content, and $(T_{37} - T_{37}^*)$ which depends on the area in the *fov* of the radiometer that has a rain rate in excess of a threshold. T_{37}^* is taken to be 15 K above the minimum brightness temperature that occurs in a given 3° latitude by 5° longitude oceanic grid box during 1 month. This brightness temperature T_{37}^* is assumed to represent the starting point for rain (PDNSL), and γ is an empirical constant.

The new parameter (dT_{37}/dT_{19}) is introduced into eq.(1) such that it modifies the effective rain area to reflect the distribution of rain types (uniform light rain or non-uniform moderate convective rain). Then T_{85} is introduced as a multiplicative exponential term. This term selectively enhances the rain rate when T_{85} is less than a particular value, such as 240 K. Reflecting these postulations, eq. (1) is changed to:

$$R = \exp[A]\exp[B] - 1 \qquad [2]$$

where:

$$A = [\beta(w)(T_{37} - T_{37}^*)]^{1.3} \frac{(T_{19} - T_{19}^*)}{(T_{37} - T_{37}^*)}$$

$$B = \begin{cases} 0 & \text{when } T_{85} > 260 \text{ K} \\ (260 - T_{85}) / 40 & \text{when } T_{85} < 260 \text{ K and } T_{37} > (T_{37}^* + 40) \\ 2.5 & \text{when } T_{85} < 180 \text{ K and } T_{37} > (T_{37}^* + 40) \end{cases}$$

Here T_{19}^* is defined analogous to T_{37}^*, w (g/cm^2) is the columnar water-vapor content, and $\beta(w) = 0.018 + .003w^{0.8}$.

The fact that the *fov* of the radiometer at the three frequencies 19- , 37- , and 85-GHz is inversely proportional to the frequencies of each channel has not been taken into consideration explicitly in the above equations. It appears that this is unimportant as long as the largest radiometer *fov*, ~60 km at 19 GHz, is at least an order of magnitude smaller than the scale of the mesoscale convective systems. Furthermore, as reflected in eq. (1), the finest *fov* of the 85-GHz channel is valuable to highlight preferentially the ice scattering effect due to tall convective rain cells that are generally not extensive, and the largest *fov* at 19 GHz helps to sense liquid hydrometeors with minimum scattering effect.

According to the ideas presented here, the spatial distribution of hydrometeors can profoundly influence the microwave brightness temperature. As a consequence, the brightness temperature can be a dual-valued function of *fov*-averaged rain rate. This dual-valued relationship is analogous to that due to scattering of radiation as suggested by Wu and Weinman, 1984.

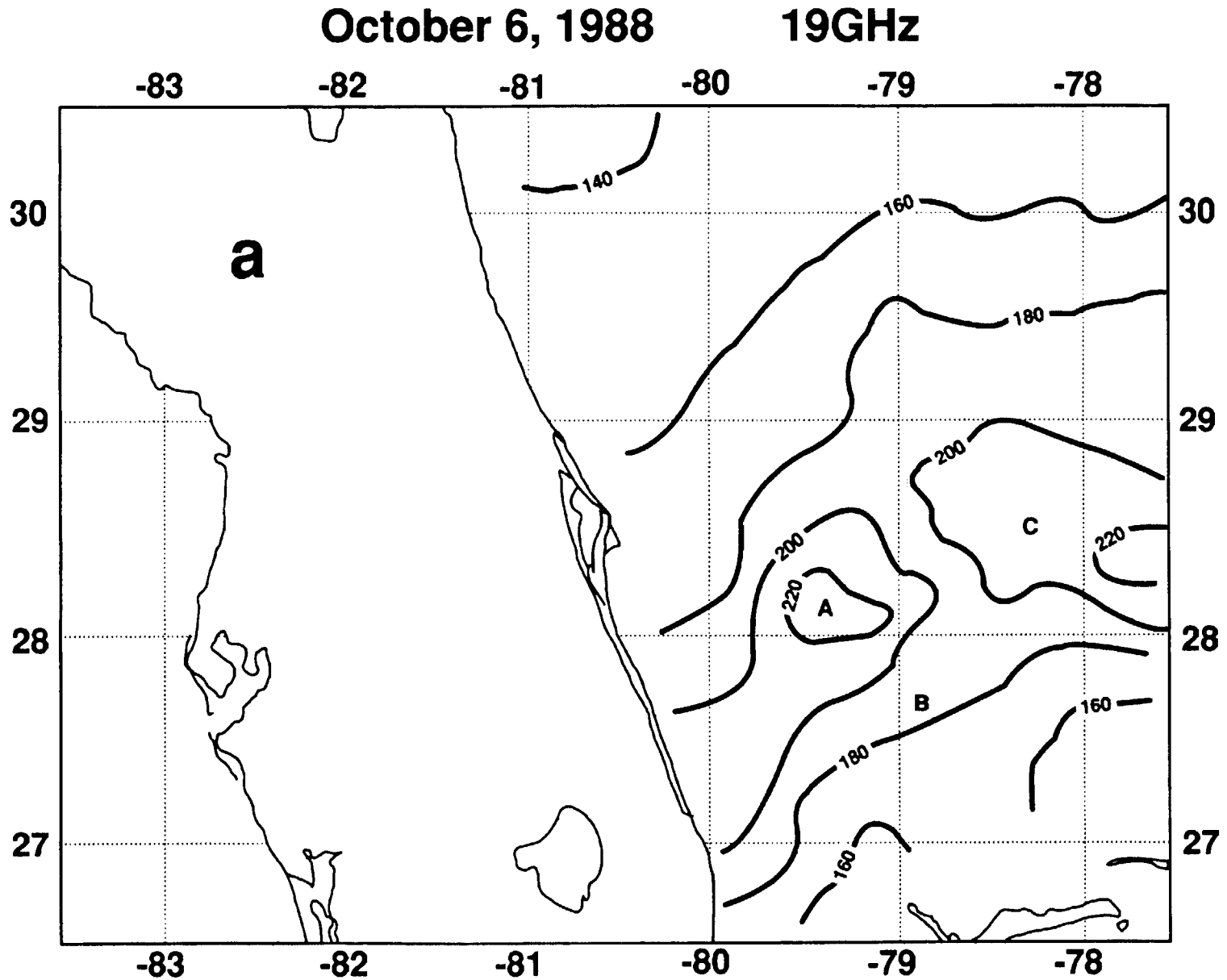

Fig. 4: Rain event of Oct. 6, 1988 (11:20 Z) over the Atlantic Ocean to the east of Florida. Analysis of SSM/I brightness temperature data. The letters A, B, and C shown in the analysis indicate local rain areas of interest.

a) 19 GHz brightness temperature, T_{19} K.

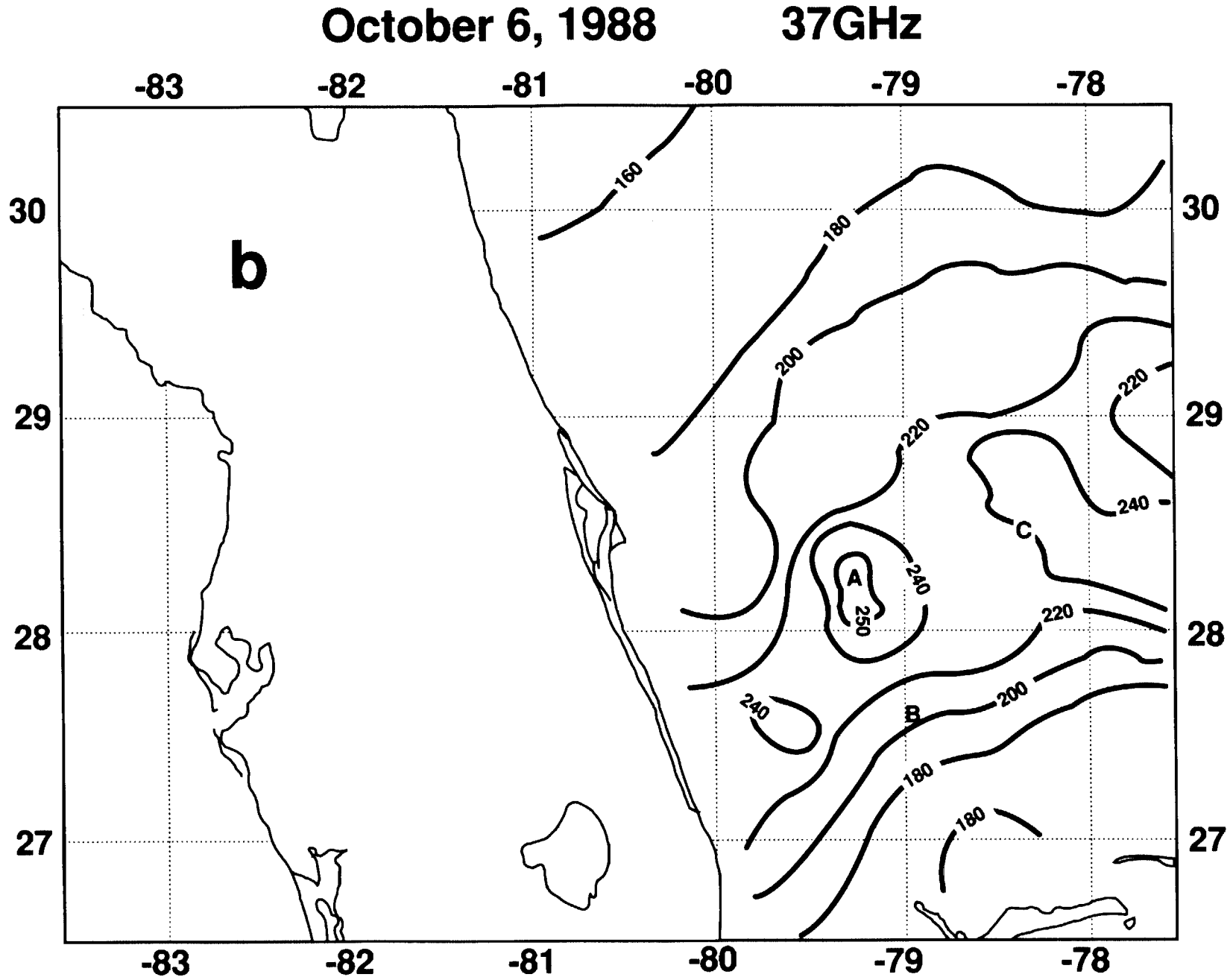

b) 37-GHz brightness temperature, T_{37} K.

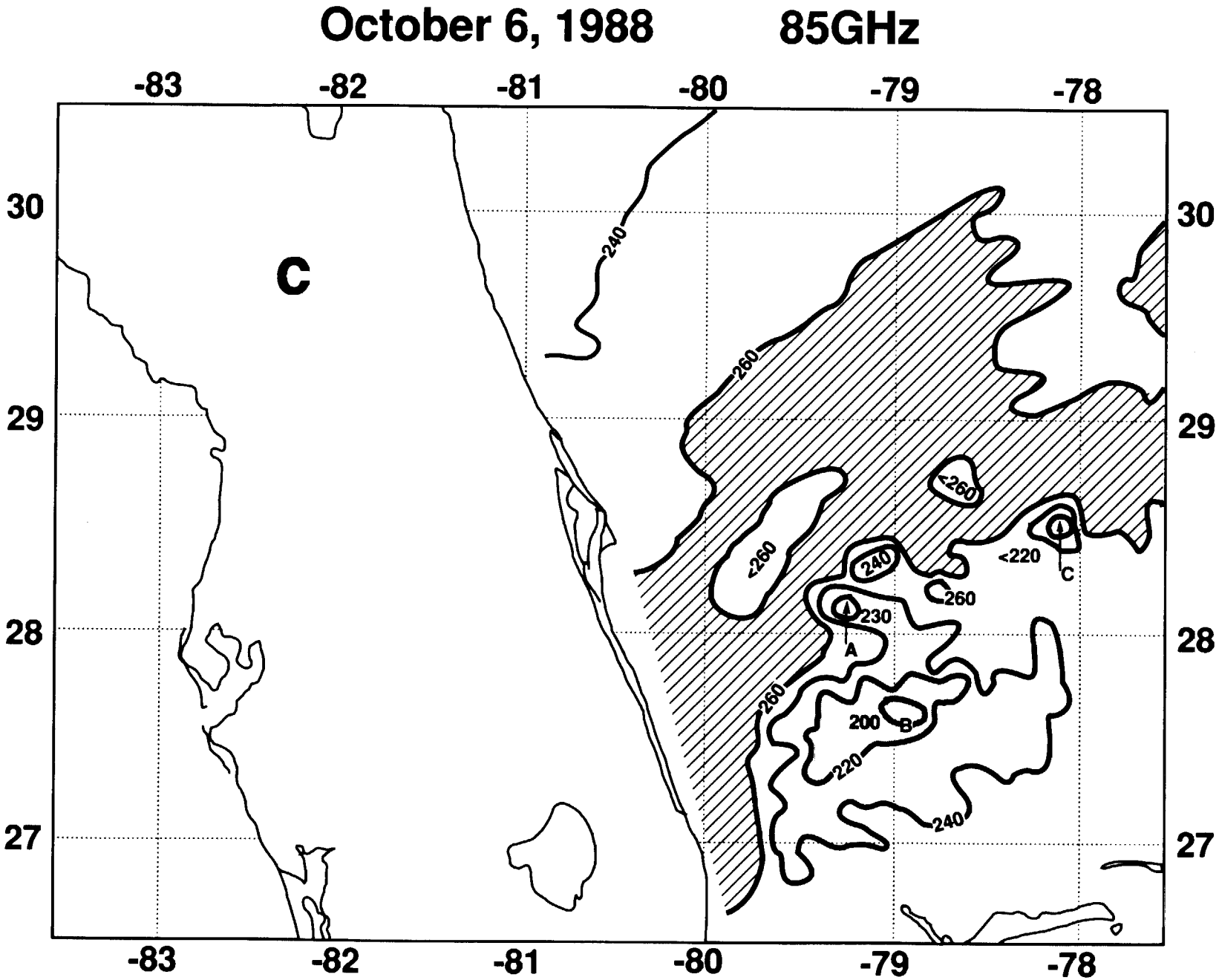

c) 85-GHz brightness temperature, T_{85} K. Regions with $T_{85} > 260$ K, representing stratiform clouds and light rain, are shown with cross hatching. Regions with $T_{85} < 240$ K, indicating strong scattering by hydrometeors, are shown by light dots.

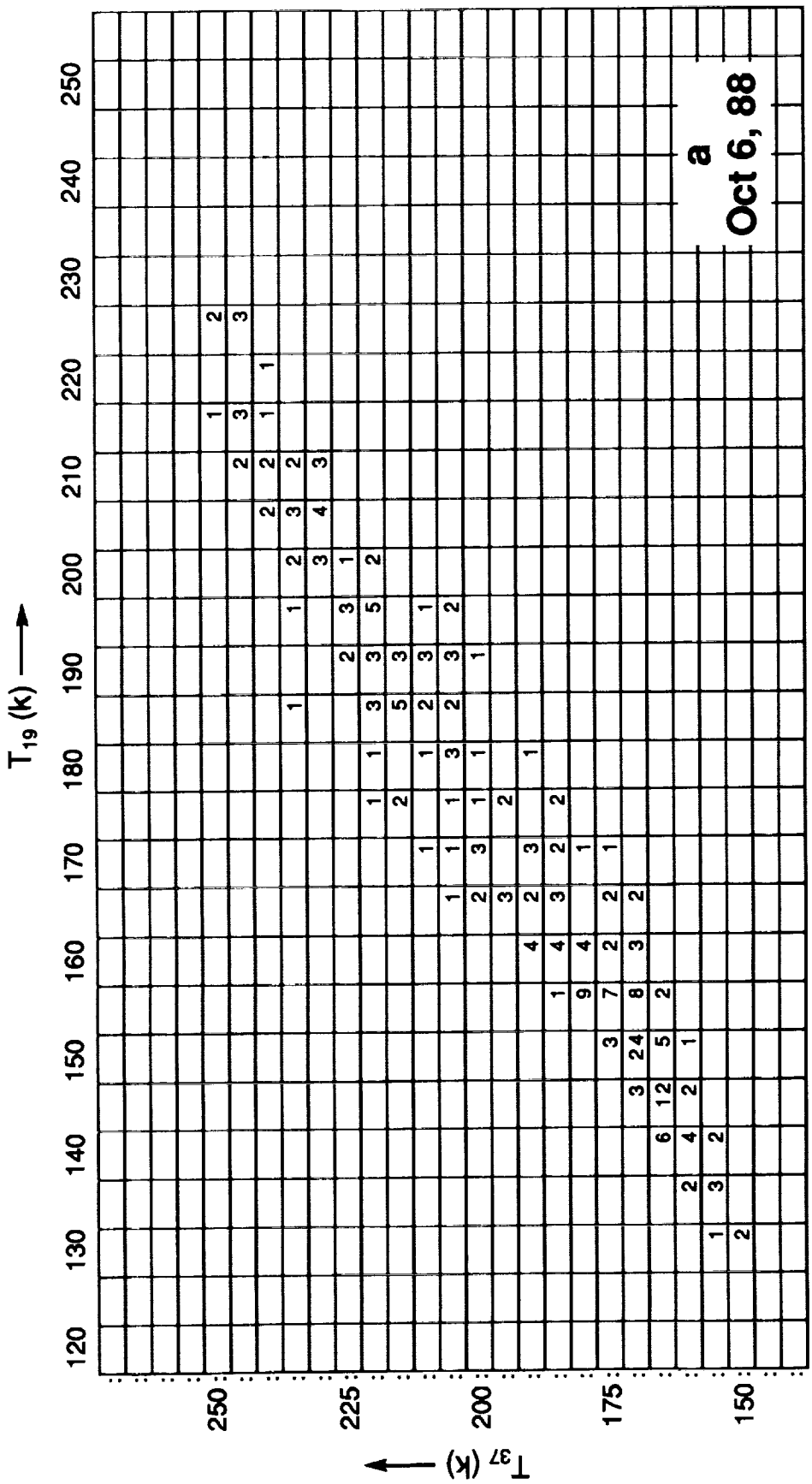

Fig. 5: Rain event of Oct. 6, 1988 (11:20 Z) over the Atlantic Ocean to the east of Florida.
a) Bi-directional histogram of SSM/I 19- and 37- GHz data.

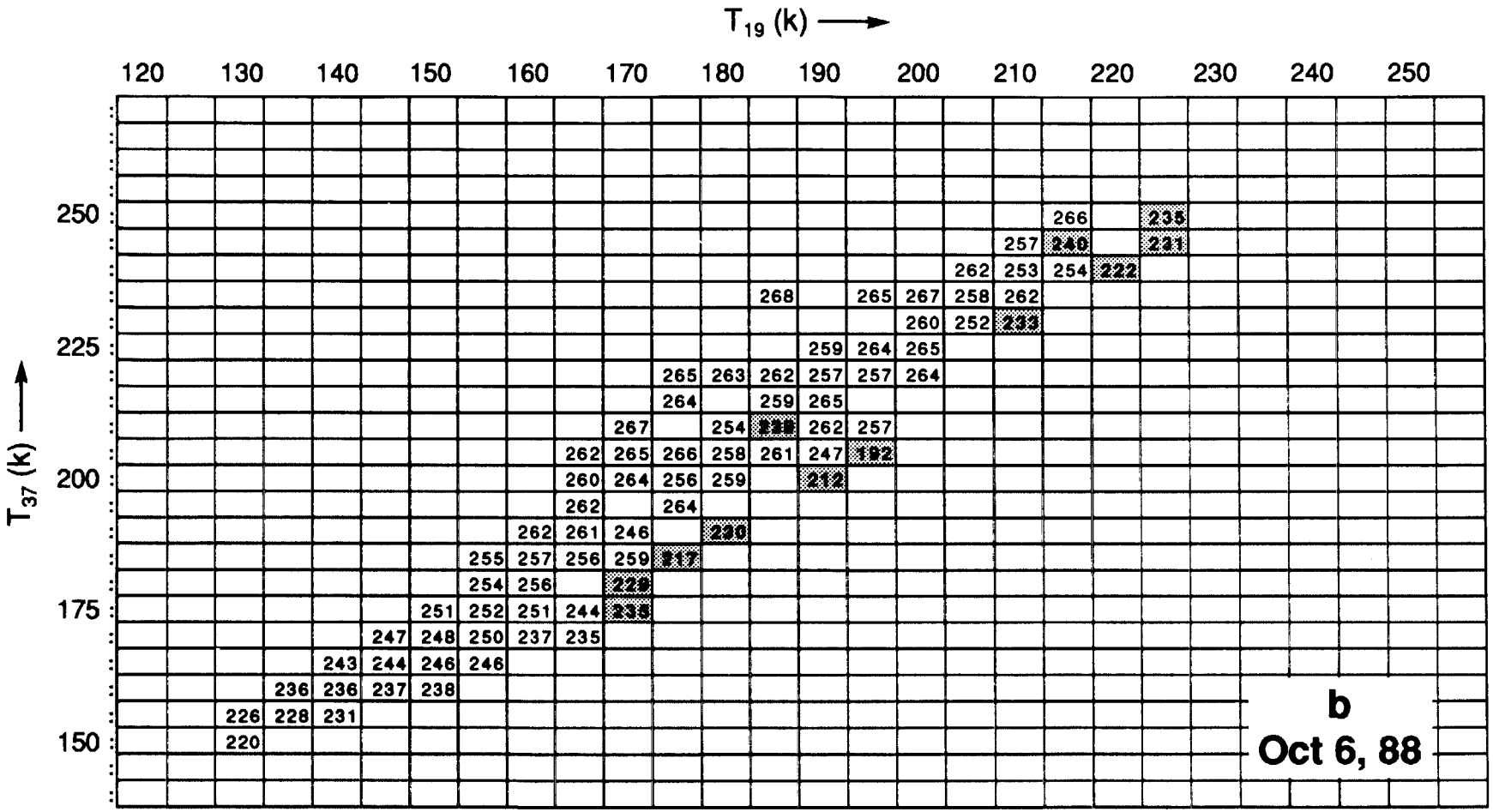

b) Mean T85 K corresponding to the bins shown in Fig. 5a. Bins with T85 < 240 K are shaded.

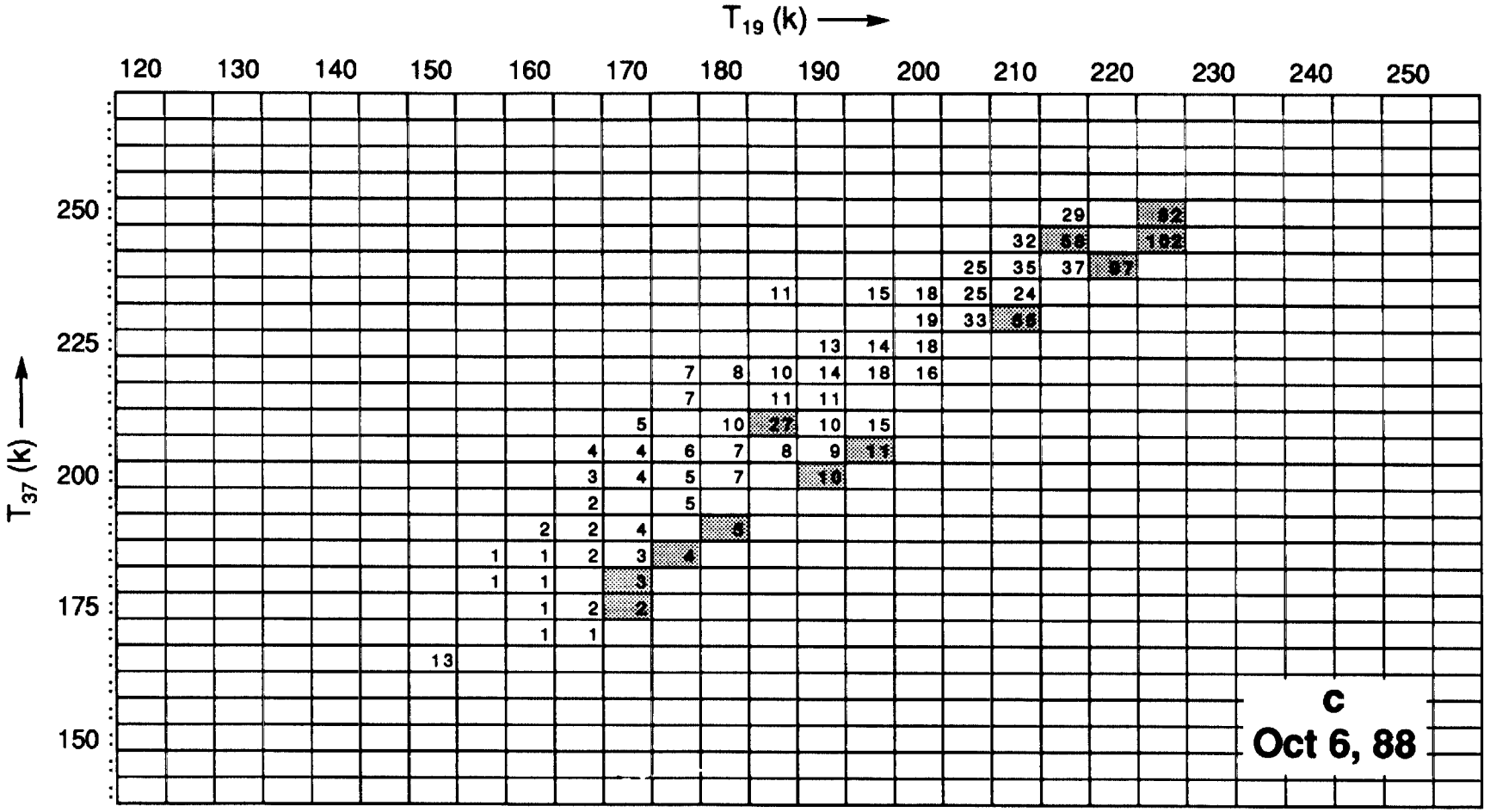

c) Rain rate (mm/h x 10) corresponding to the bins shown in Fig. 5a. Bins with T85 < 240 K are shaded.

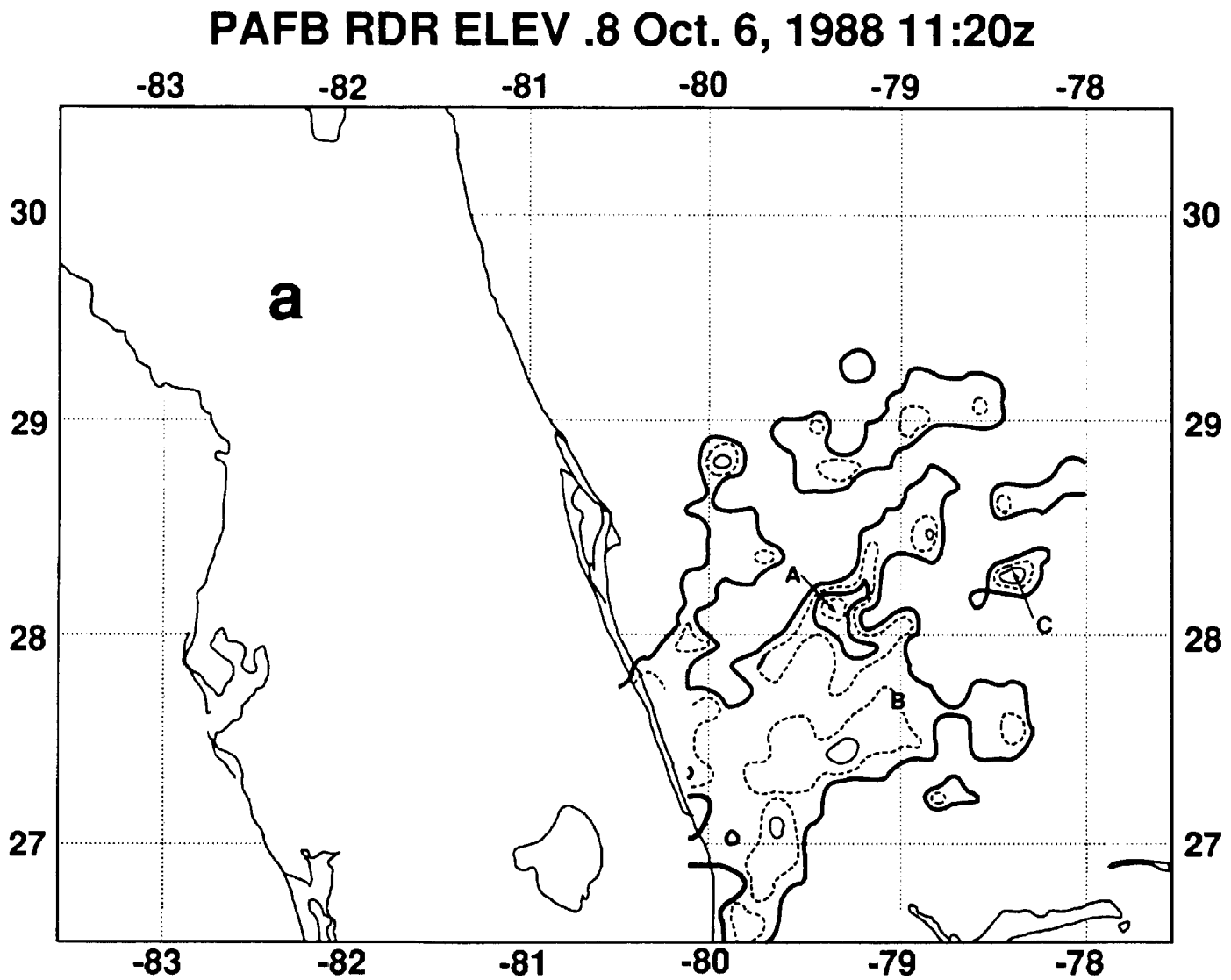

Fig. 6: Rain event of Oct. 6, 1988 (11:20 Z) over the Atlantic Ocean to the east of Florida. Letters A, B, and C, adopted from Fig. 4, indicate local rain areas of interest.

a) Patrick AFB radar back-scatter data at 20, 25, 30, and 35 dBz levels. The outermost contour is for 20 dBz. The innermost contour includes all levels greater than 35 dBz.

Taking dBz = 10 $\log_{10}$ Z; Z = 230 $R^{1.25}$; where Z is the radar back-scatter and R is the rain rate in mm/h, the four dBz levels given above correspond to rain rates of 0.5, 1.3, 3.2, and 8.1 mm/h.

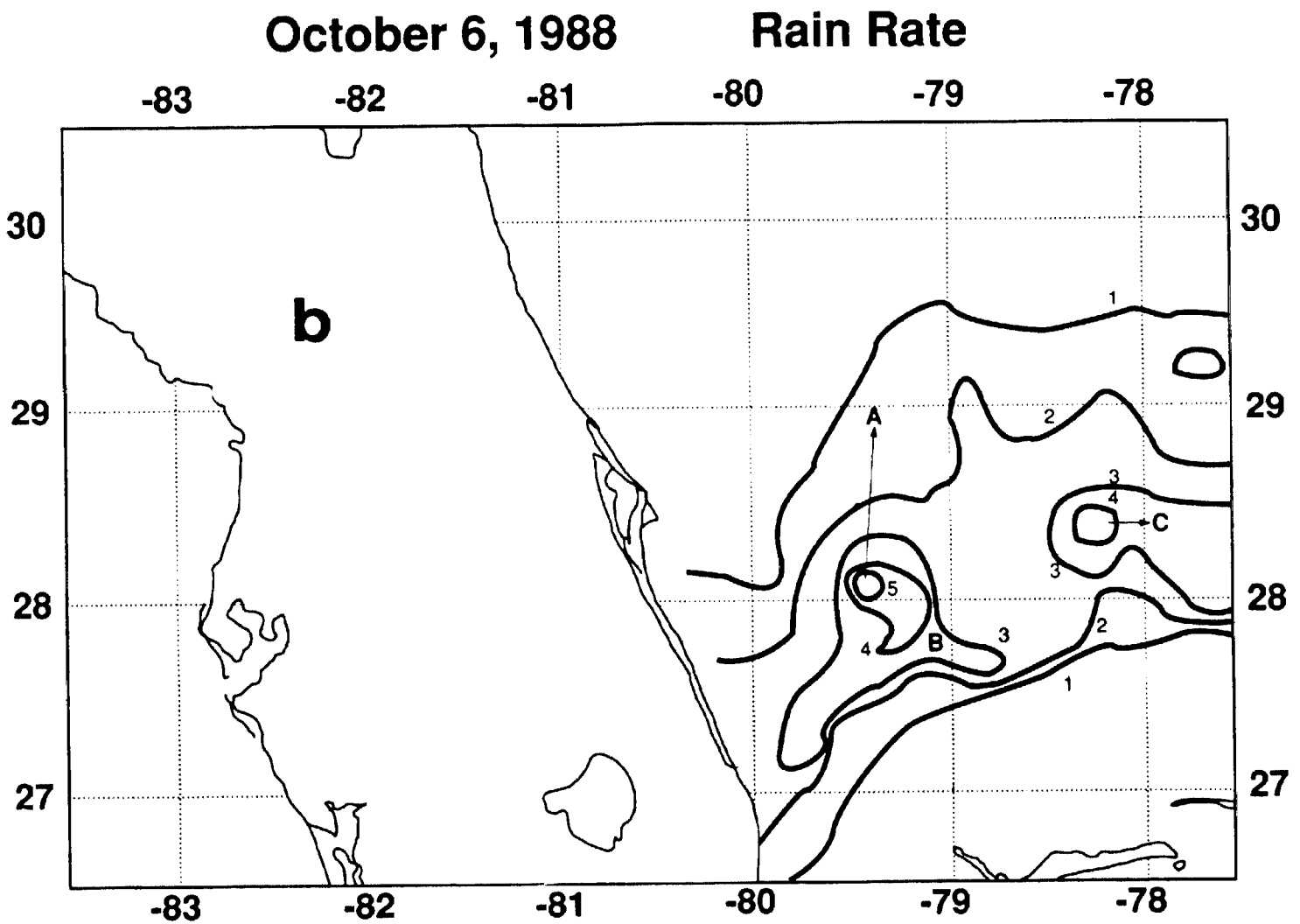

Fig. 6: Rain event of Oct. 6, 1988 (11:20 Z) over the Atlantic Ocean to the east of Florida. Letters A, B, and C, adopted from Fig. 4, indicate local rain areas of interest.

b) Rain rate (mm/h) deduced from SSM/I 19-, 37-, and 85-GHz data. The contours labeled 1, 2, 3, 4, and 5 indicate rain rates of 0.5, 1.3, 3.2, 8.1, and 14.1 mm/h.

Case Studies

The microwave rain rate retrieval model developed here is applied to two rain events, Jan. 25, 1988 (00:04Z), and Oct. 6, 1988 (11:20Z), over the Atlantic to the east of Florida. The rain rates deduced from Patrick Air Force Base radar backscatter data that are not calibrated against rain gauges are used as ground truth for these two cases. These cases illustrate the applicability of the rain retrieval model to different seasons.

Fig. 4a, b, and c, show analysis of the brightness temperature measurements made by SSM/I to the east of Florida on Oct. 6, 1988 at 19- , 37- , and 85-GHz. The **bdh** of the T_{19} and T_{37} data is shown in Fig. 5a. The mean T_{85} corresponding to each one of the bins is shown in Fig. 5b. The rain rate for each of the bins calculated according to eq. (2) is shown in Fig. 5c. One notices the rain rate increases along the abscissa and ordinate, and more strikingly whenever there is a low value of T_{85}. Also, as expected from eq. (2), increase in rain rate along the abscissa, i.e. dependence on T_{19}, is more pronounced than the increase along the ordinate. A map containing analysis of the Patrick AFB radar backscatter signal for the Oct. 6 case is shown in Fig. 6a. The radar signal can be readily converted to rain rate, as indicated in the figure, assuming a Z-R relationship. A map of the corresponding SSM/I-derived rain rates is shown in Fig. 6b. Although there are some inherent problems in comparing the radar rain data with the satellite retrievals (due to resolution, bright band, attenuation, curvature of the earth—see e.g., Atlas *et al.*, 1990; Petty and Katsaros, 1990) we can notice a broad agreement between the two results. In particular, one may note the agreement in position and rain intensity at two locations, A and C, shown in these figures. At these locations, the T_{85} data indicate strong centers of scattering due to hydrometeors. At location B, we note from our rain retrievals shown in Fig. 6b that there is a rapid transition from intense rain to light rain. Although the T_{85} data at location B suggest a scattering center, the T_{19} and T_{37} data that do not have the same resolution show only low values of 190 and 205 K, respectively, at this location. In addition, radar data at B do not suggest a strong backscatter signal. Therefore we believe the strong T_{85} scattering signal at B is very likely associated with ice particles from defunct convective cells that are drifting with the mean wind. The ice particles do not produce a strong radar backscatter signal but lead to strong scattering at 85.5 GHz.

In Figures 7 (a, b, and c), 8 (a, b, and c), and 9 (a and b), all the satellite and radar data (including analysis) that are similar to the earlier case study are presented for the Jan. 25, 1988 rain event. Here we find there is the problem of

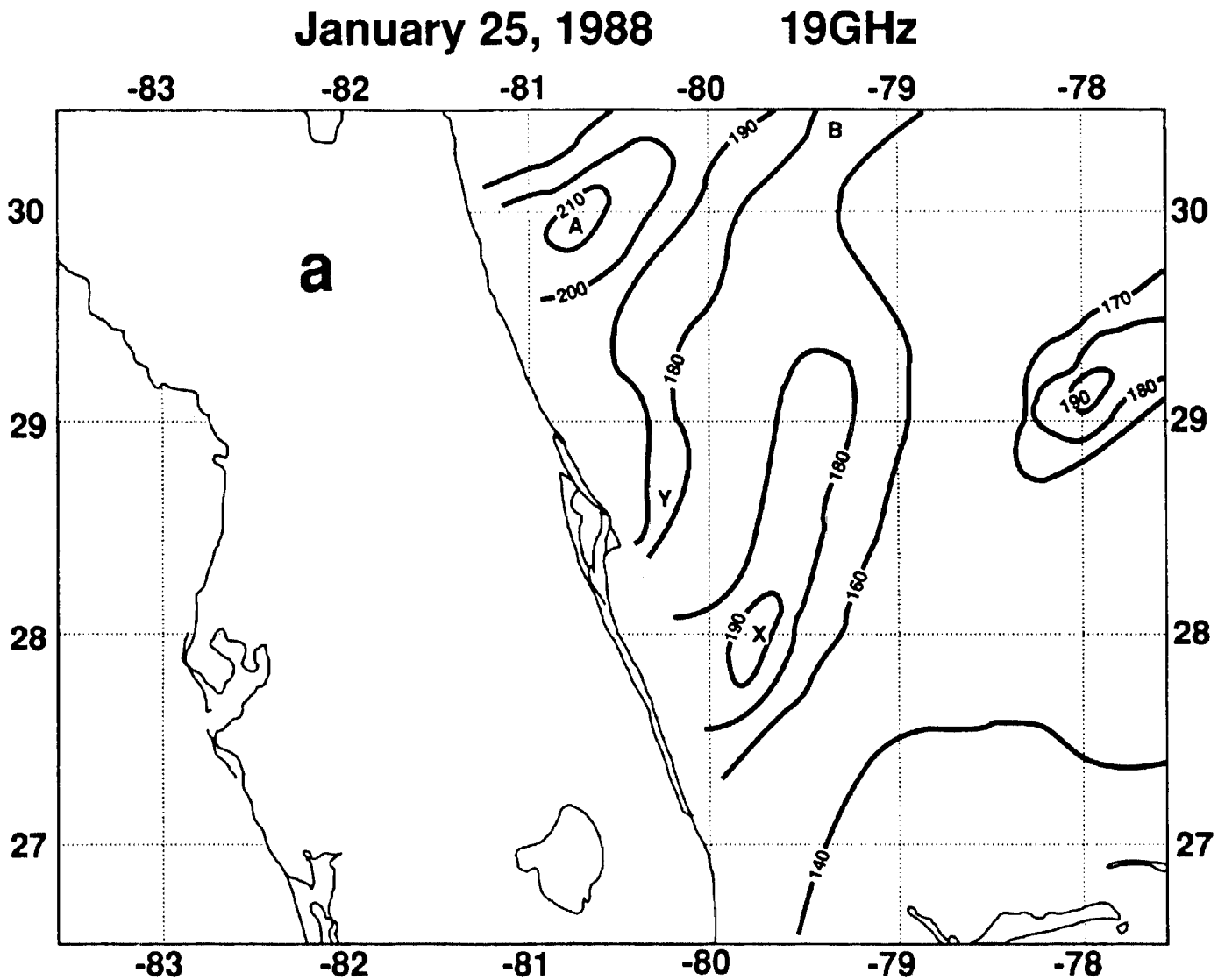

Fig. 7: Rain event of Jan. 25, 1988 (00:04 Z) over the Atlantic Ocean to the east of Florida. Analysis of SSM/I brightness temperature data. The letters A, B, X, and Y shown in the analysis indicate local rain areas of interest.

a) 19 GHz brightness temperature, T_{19} K.

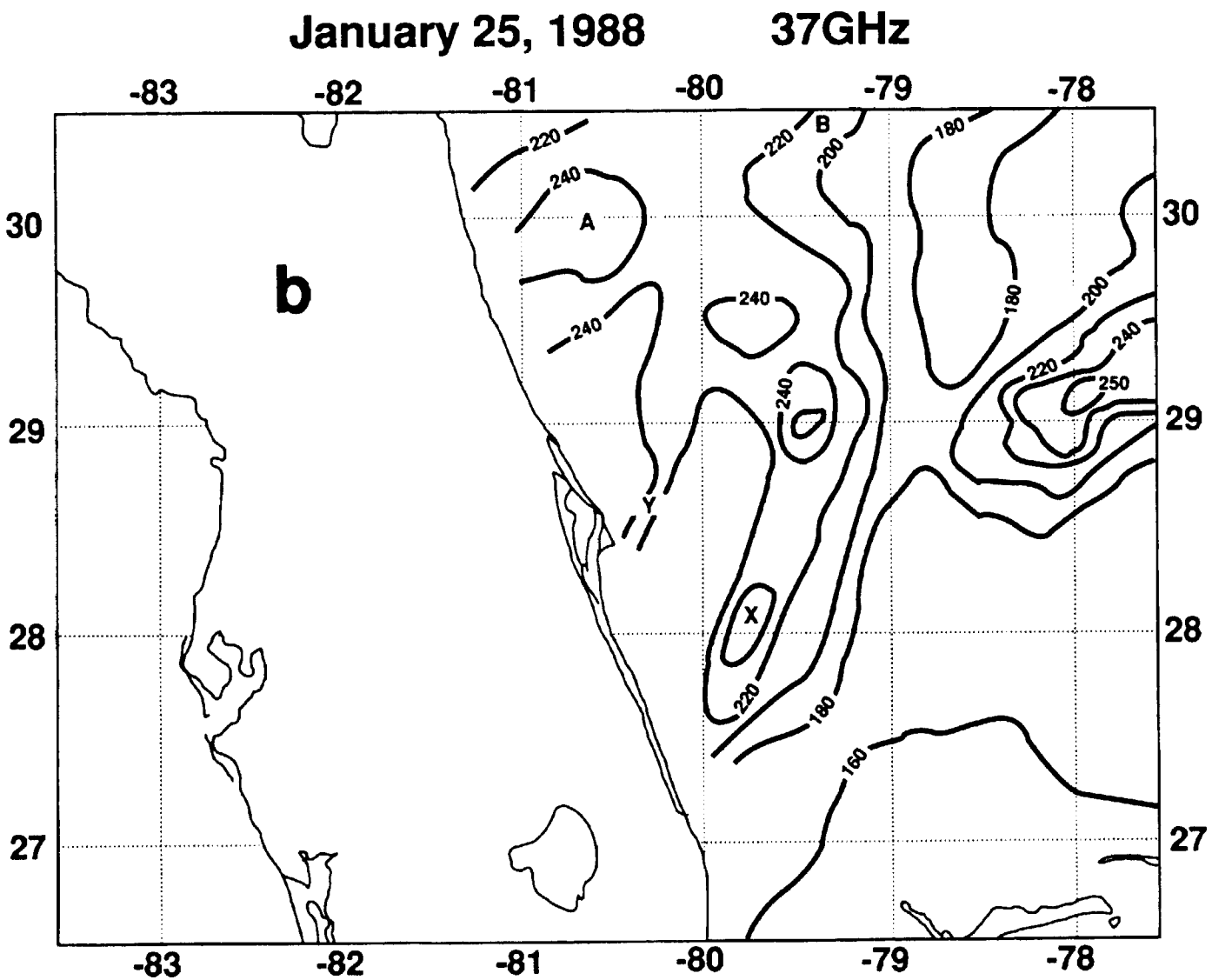

b) 37 GHz brightness temperature, T_{37} K.

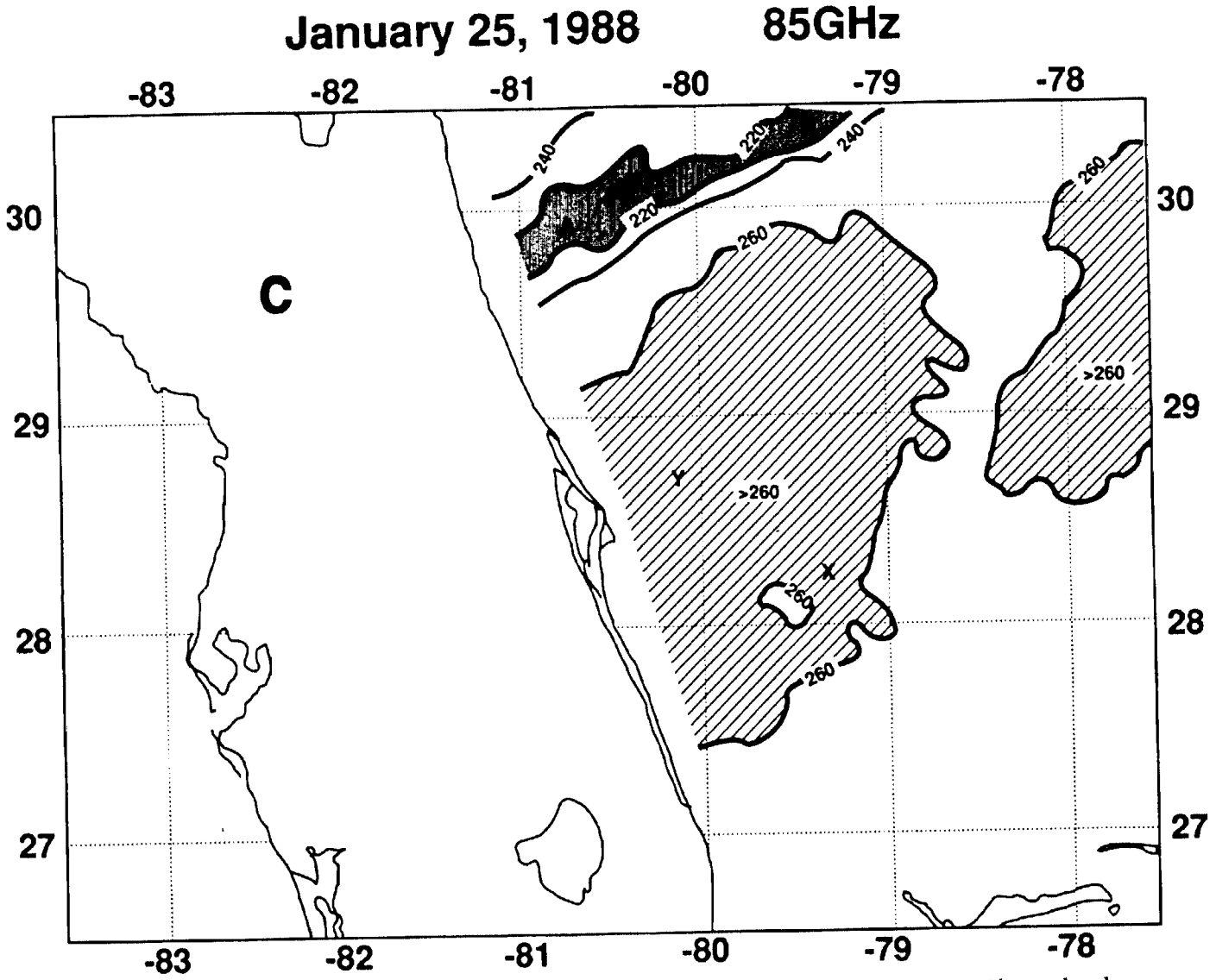

c) 85 GHz brightness temperature, T_{85} K. Regions with $T_{85} > 260$ K, representing stratiform clouds and light rain, are shown with cross hatching. Regions with $T_{85} < 240$ K, indicating strong scattering by hydrometeors, are shown by light dots.

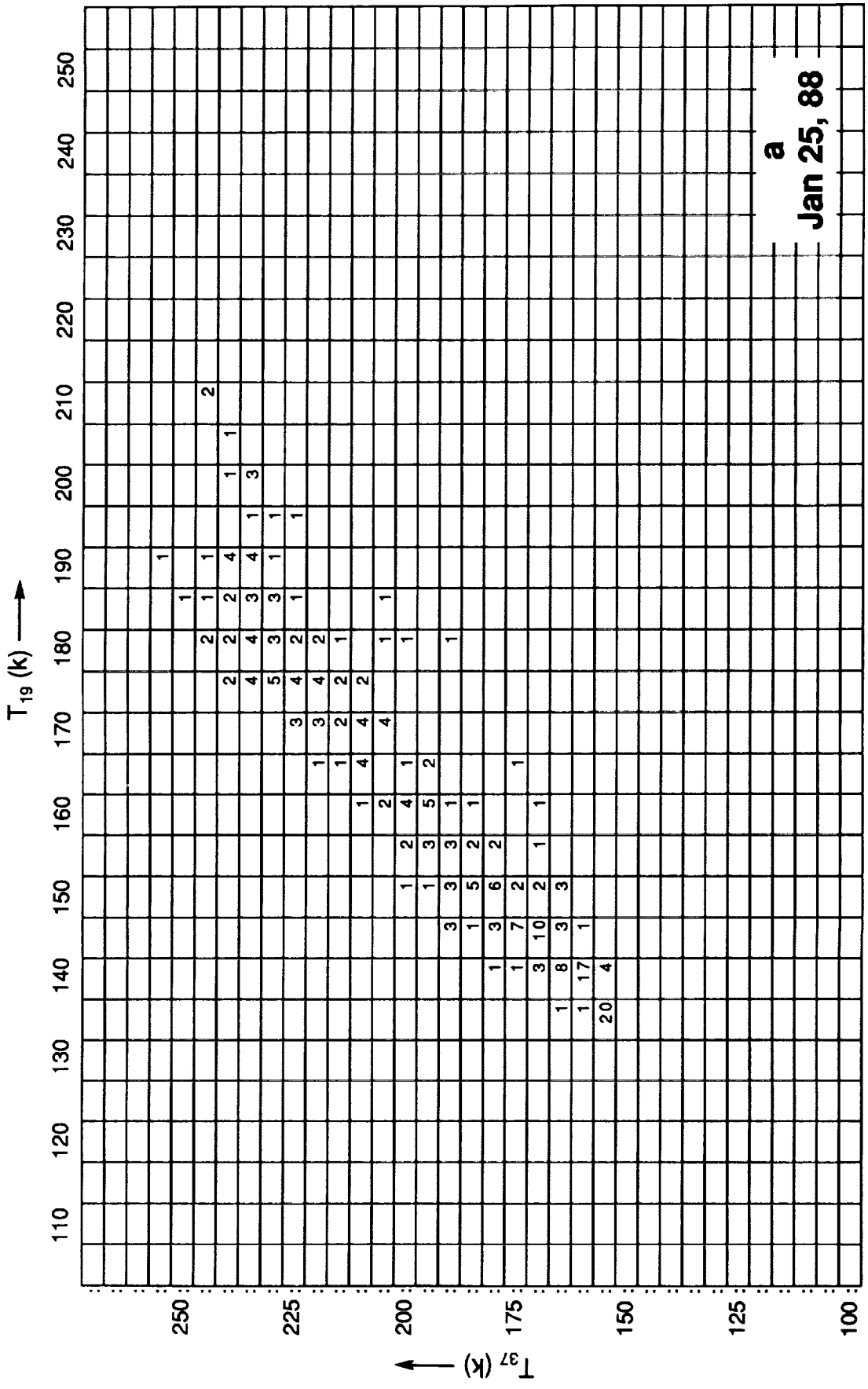

Fig. 8: Rain event of Jan. 25, 1988 (00:04 Z) over the Atlantic Ocean to the east of Florida.
a) Bi-directional histogram of SSM/I 19- and 37- GHz data.

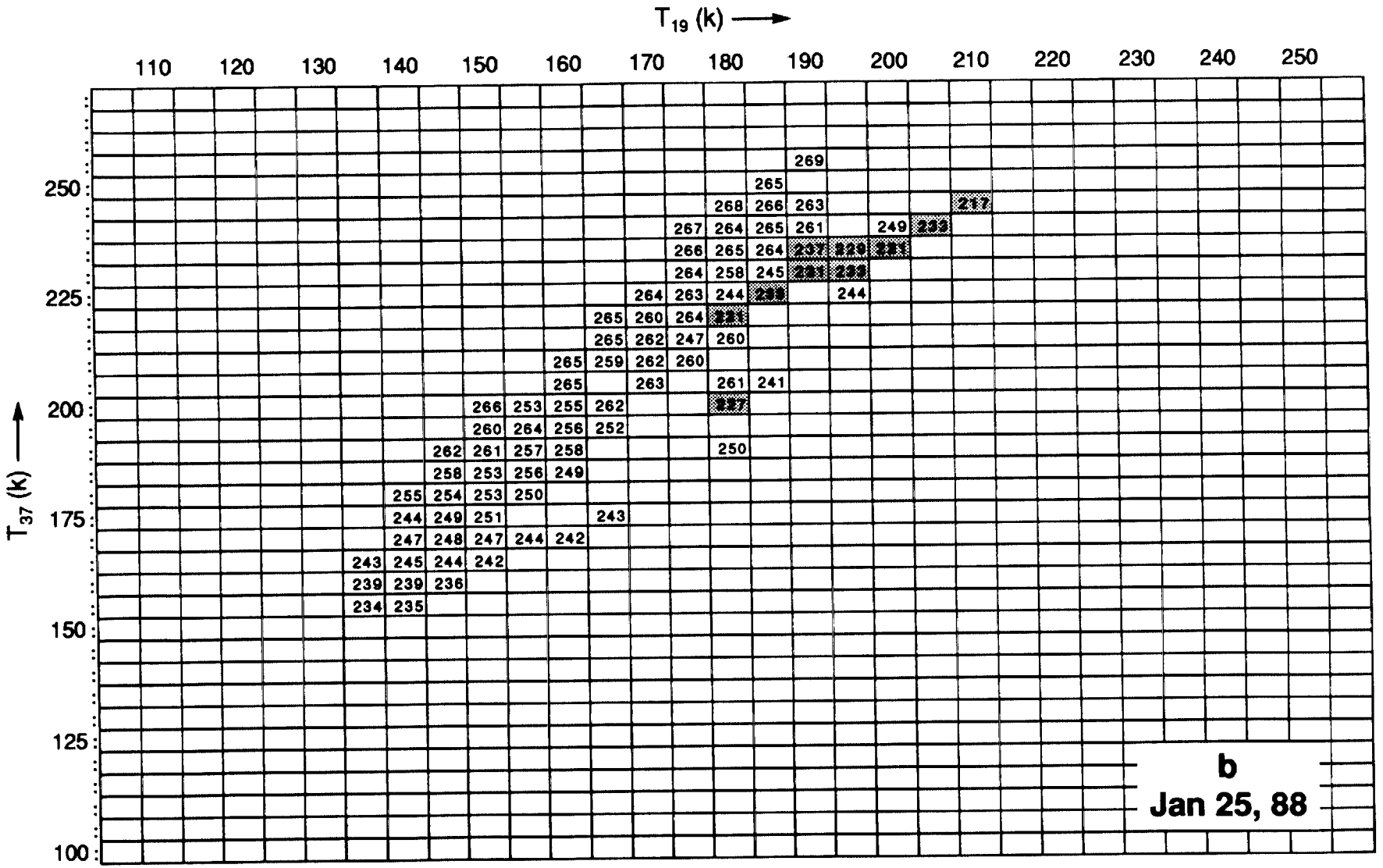

b) Mean T_{85} K corresponding to the bins shown in Fig. 5a. Bins with $T_{85} < 240$ K are shaded.

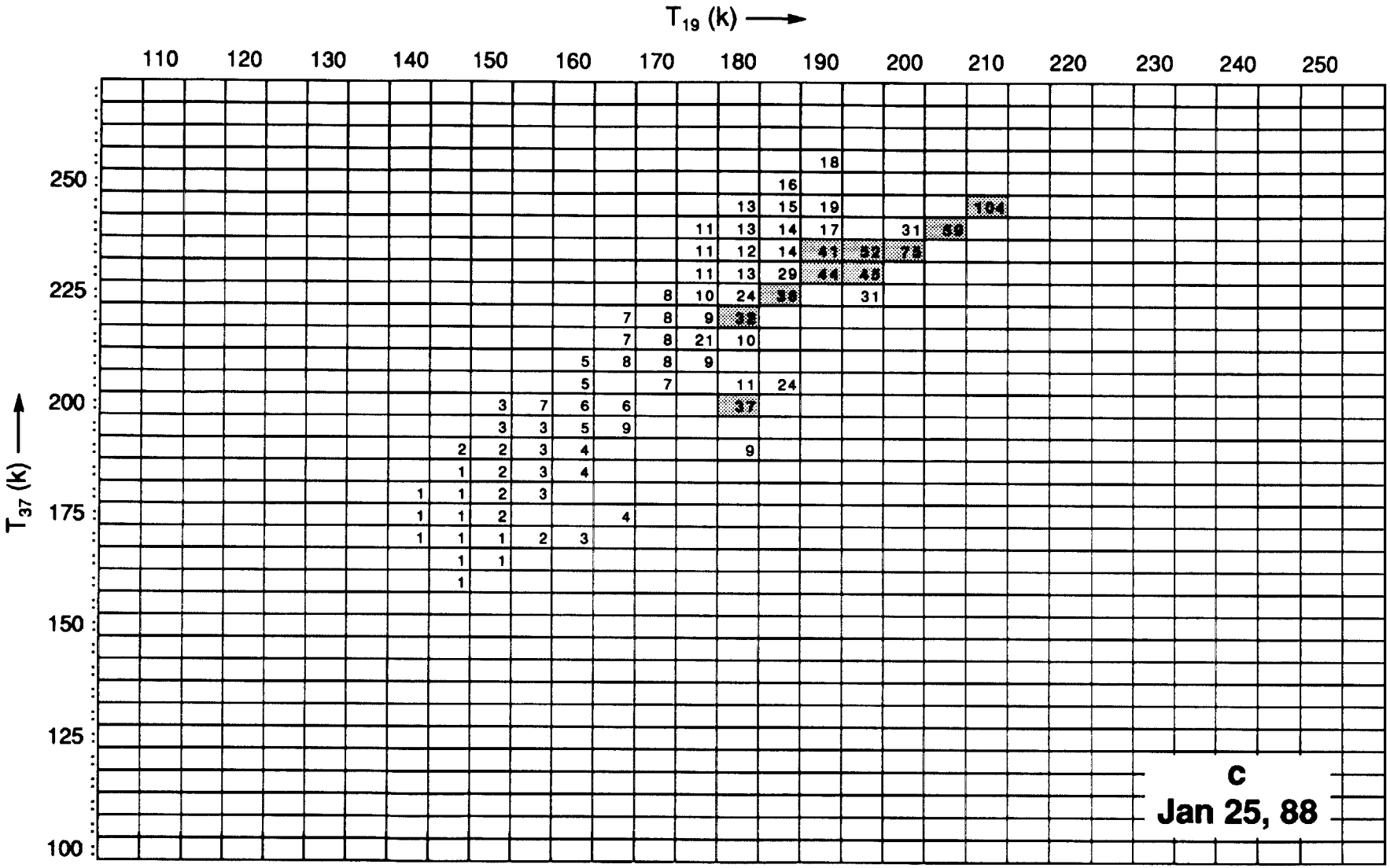

c) Rain rate (mm/h x 10) corresponding to the bins shown in Fig. 5a. Bins with T_{85} < 240 K are shaded.

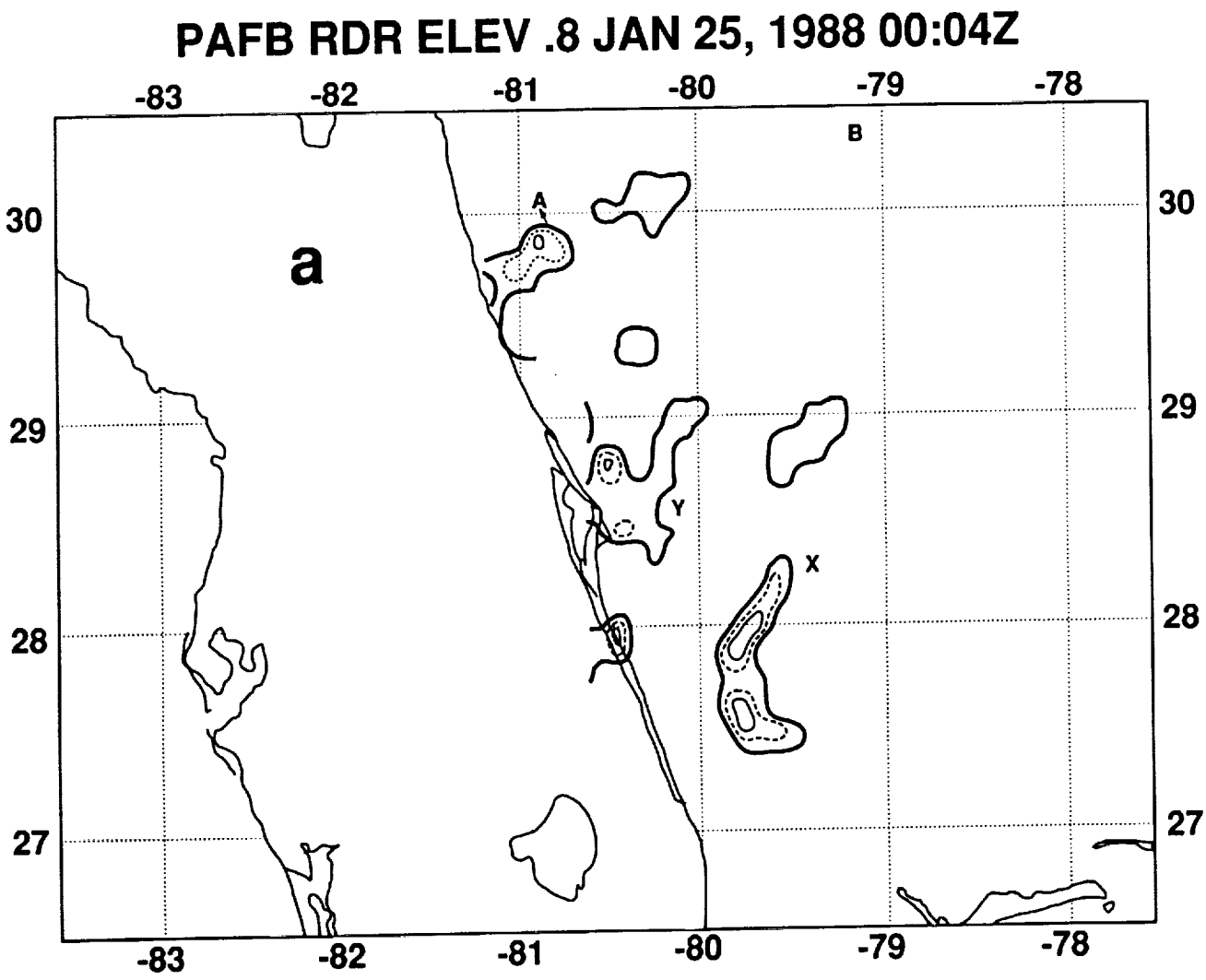

Fig. 9: Rain event of Jan. 25, 1988 (00:04 Z) over the Atlantic Ocean to the east of Florida. Letters A, B, X, and Y, adopted from Fig. 7, indicate local rain areas of interest.

a) Patrick AFB radar back-scatter data at 20, 25, 30, and 35 dBz levels. The outermost contour is for 20 dBz. The innermost contour includes all levels greater than 35 dBz.

Taking $dBz = 10 \log_{10} Z$; $Z = 230\ R^{1.25}$; where Z is the radar back-scatter and R is the rain rate in mm/h, the four dBz levels given above correspond to rain rates 0.5, 1.3, 3.2, and 8.1 mm/h.

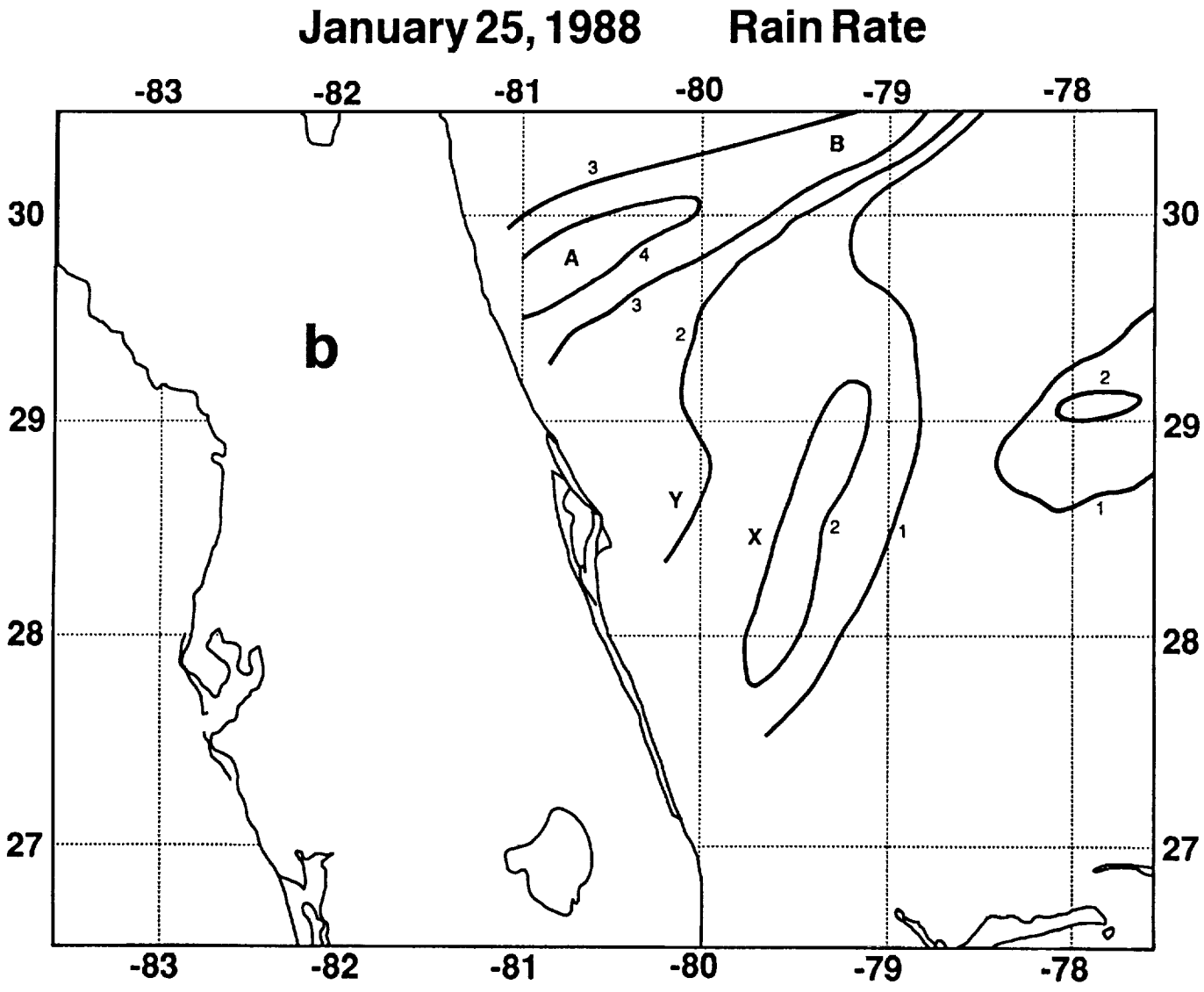

b) Rain rate (mm/h) deduced from SSM/I 19-, 37-, and 85- GHz data.

the "bright band," produced by a thin, melting layer of ice particles in stratiform rain (Ramanamurthy *et al.*, 1965; Kummerow *et al.*, 1989) that can enhance the radar backscatter at the locations X and Y (see Fig. 9a). The 85-GHz brightness temperature data (Fig. 7c) do not respond very well to this bright band. At the location X, there is only a weak indication of scattering at T_{85}. Based on the T_{85} map, we suggest that there are very extensive stratiform cloud sheets indicating $T_{85} \approx 260$ K in the region 28° to 30° N and 80.5° to 79° W. In this stratiform region, the 19- and 37-GHz data lead us to infer a weak rain rate of 1 to 2 mm/h. On the other hand, at locations A and B shown in Figs. 7, 8, and 9, the SSM/I data at 19- , 37- , and 85-GHz enables us to infer significant convective rain rates that are in excess of ~ 4 mm/h.

The two case studies presented above demonstrate that we can deduce stratiform and convective rain with the help of 19-, 37-, and 85- GHz data. The intense convective rain is vividly manifested by the scattering effect in the 85 GHz data. It should be realized that sometimes the 85 GHz scattering from drifting anvils associated with decaying convective cells could be misleading.

From the above discussions we conclude that the 85 GHz data, the radar backscatter measurements, and the data from the 19- and 37- GHz channels do not convey the same information. The two case studies presented above show their independence. When all these measurements are available simultaneously, such as in the TRMM mission, one can derive rain information that will be significantly superior.

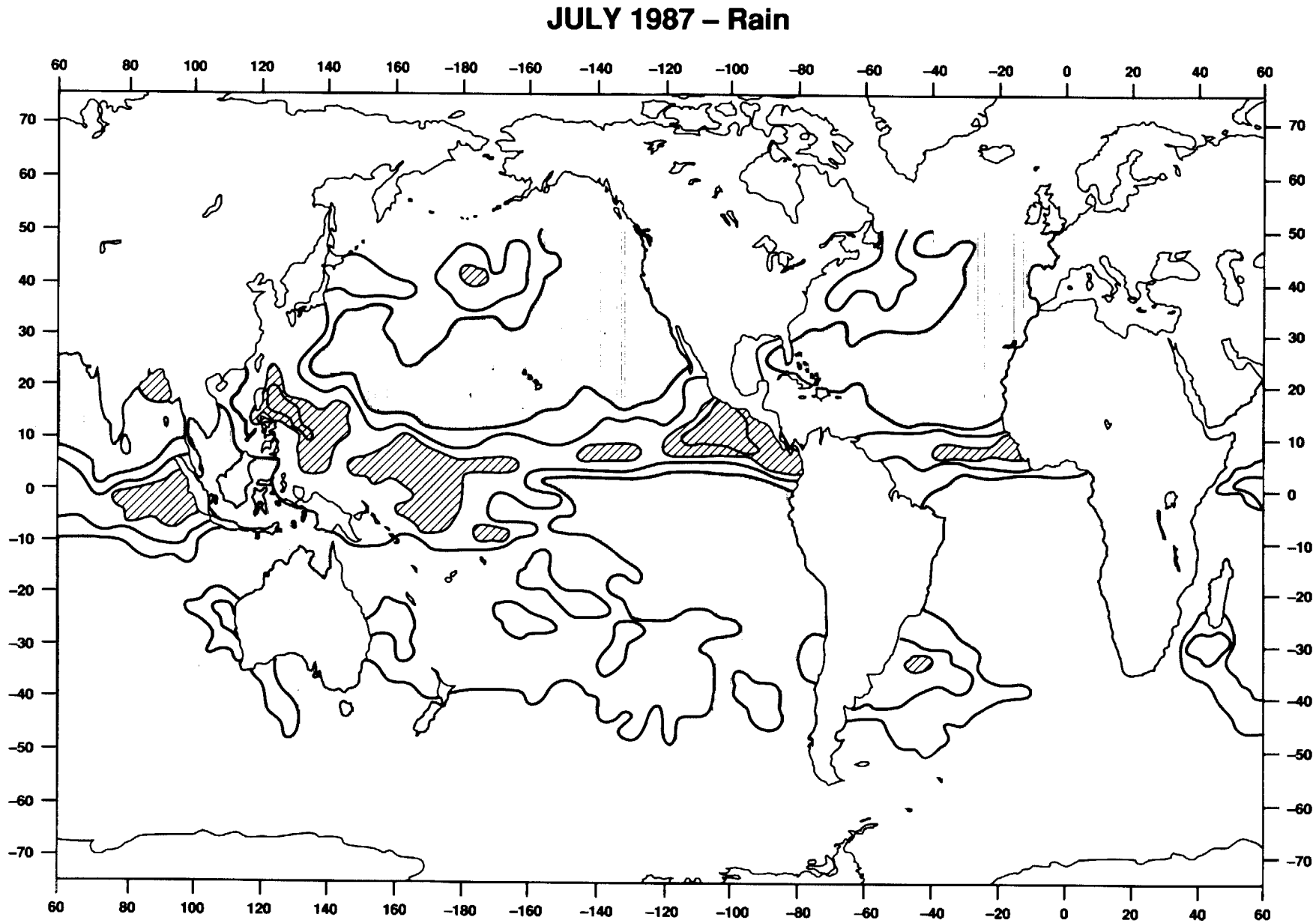

Fig. 10: a) Monthly mean rain rate (mm/h x 100) derived from SSM/I July 1987 measurements at 19, 37, and 85 GHz. Rain rate contours are shown for 0.1, 0.2, 0.4, 0.8 mm/h. Oceanic areas with shading have less than 0.1 mm/h and cross-hatched areas have greater than 0.4 mm/h rain rate.

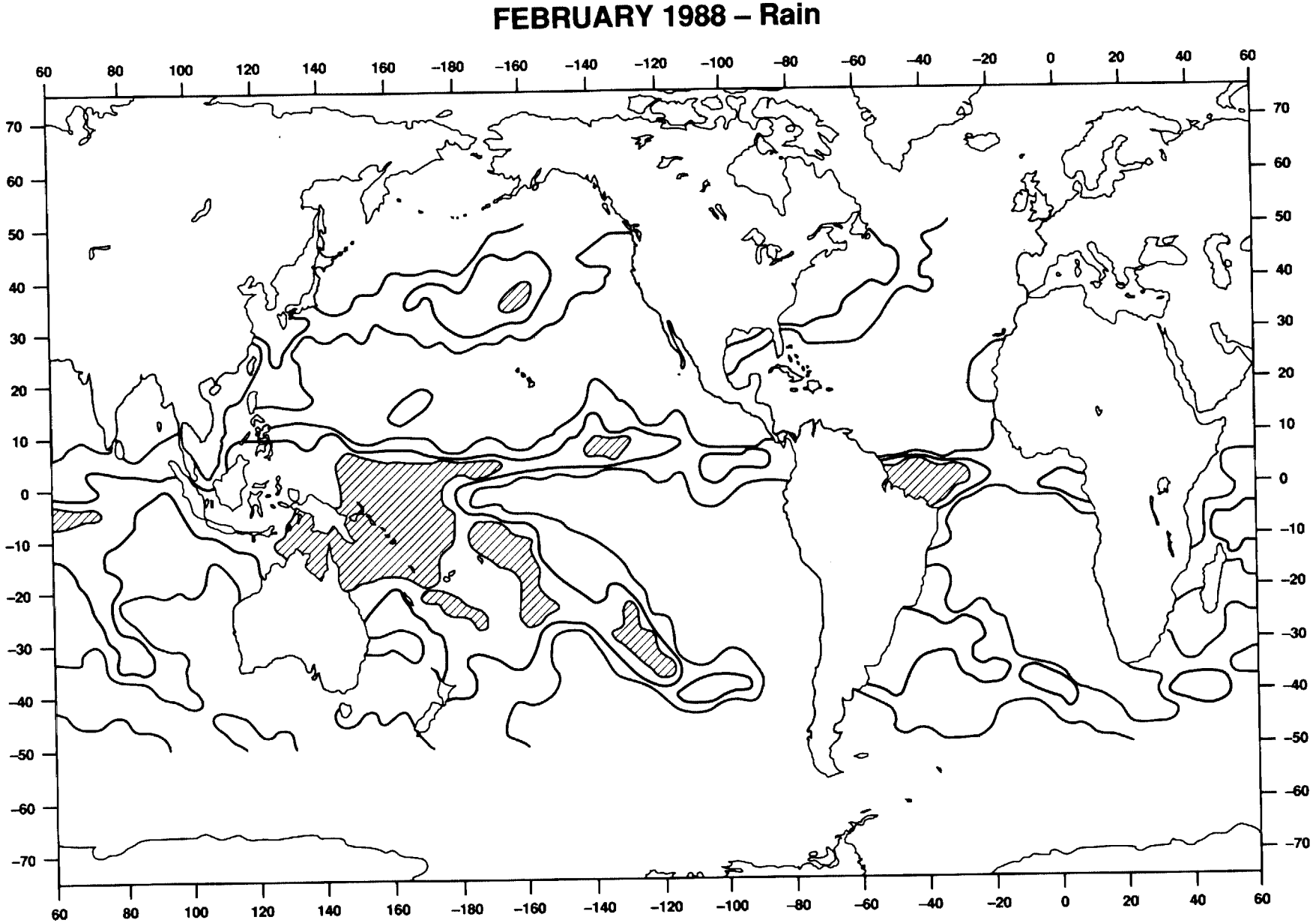

Fig. 10: b) Monthly mean rain rate (mm/h x 100) derived from SSM/I Feb. 1988 measurements at 19, 37, and 85 GHz. Rain rate contours are shown for 0.1, 0.2, 0.4, 0.8 mm/h. Oceanic areas with shading have less than 0.1 mm/h and cross-hatched areas have greater than 0.4 mm/h rain rate.

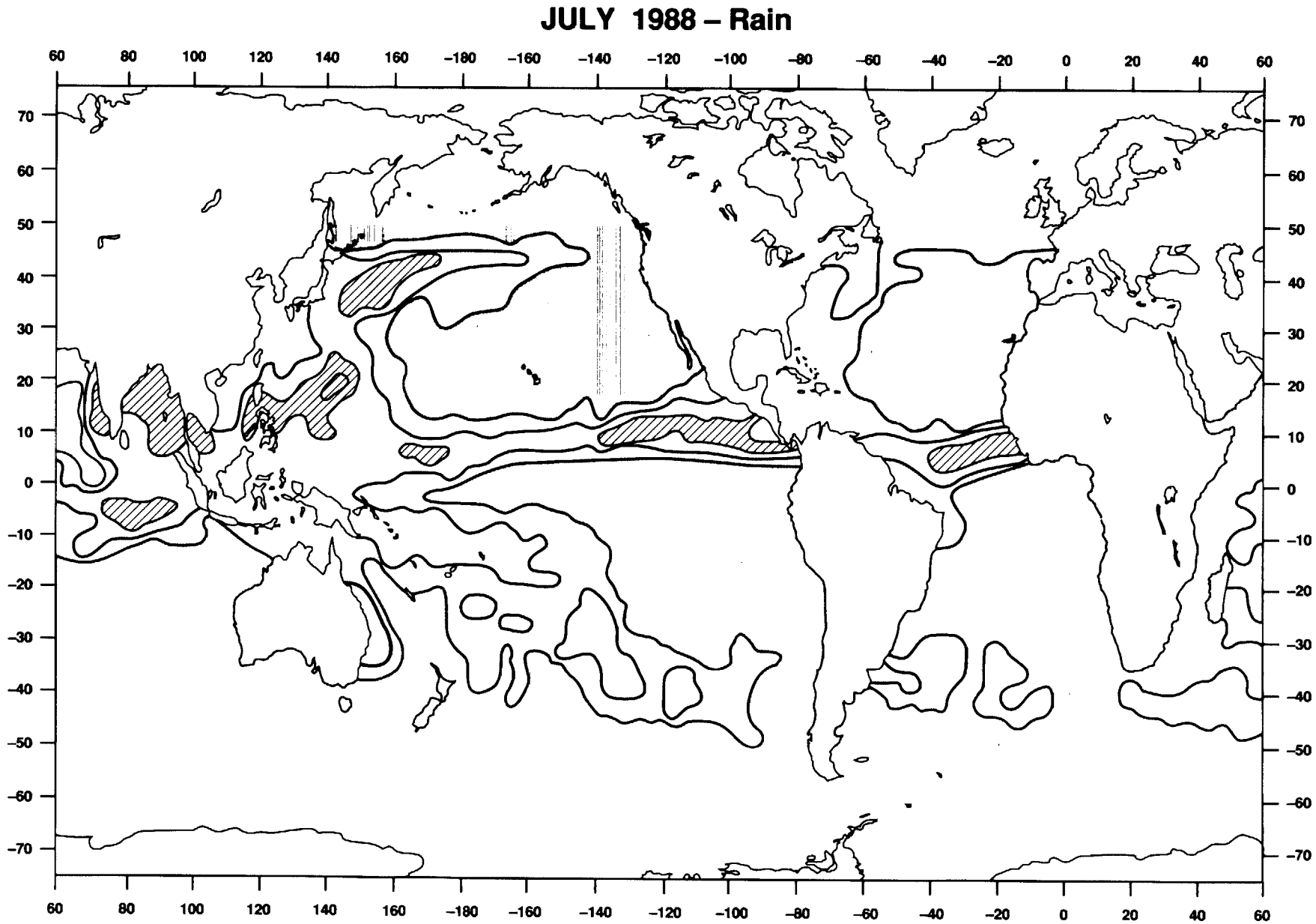

Fig. 10: c) Monthly mean rain rate (mm/h x 100) derived from SSM/I July 1988 measurements at 19, 37, and 85 GHz. Rain rate contours are shown for 0.1, 0.2, 0.4, 0.8 mm/h. Oceanic areas with shading have less than 0.1 mm/h and cross-hatched areas have greater than 0.4 mm/h rain rate.

5. Global Monthly Mean Distribution of Rainfall Over Oceans

Interannual and seasonal variations of rainfall over oceans can be an important diagnostic tool for global change studies. Passive-microwave remote sensing of rain from satellites is valuable for this purpose. In order to demonstrate this capability, we are showing three monthly mean maps of rainfall over oceans. The months of July 1987 and February 1988 are chosen to show the seasonal change, and July 1988 is selected to contrast with July 1987. These July months correspond to early and late phases of El Niño.

In Fig. 10 a, b, and c, the SSM/I-derived monthly mean rain rate over oceans from 50° N to 50° S for the three months are shown. The important rain belts—the Inter Tropical Convergence Zone (ITCZ), South Pacific convergence zone, and the rain belts along the Gulf Stream, Kuroshio, and Brazil currents—are all clearly represented in these maps. The dry subtropical subsidence areas along the eastern sectors of the oceans are vividly seen. These maps are in broad agreement with those of Dorman and Bourke (1979; 1981). Zonal mean rainfall for the Atlantic and Pacific oceans deduced from these maps are shown in Figs. 11 a, b, and c. By comparing the zonal means from the July and February maps, we can appreciate the seasonal differences. Similarly, zonal means from July 1987 to July 1988 reveal the El-Niño effect.

The precipitation in the form of snow that may occur over high latitudes during the winter season is not accounted for in our maps. This remains as a future research project.

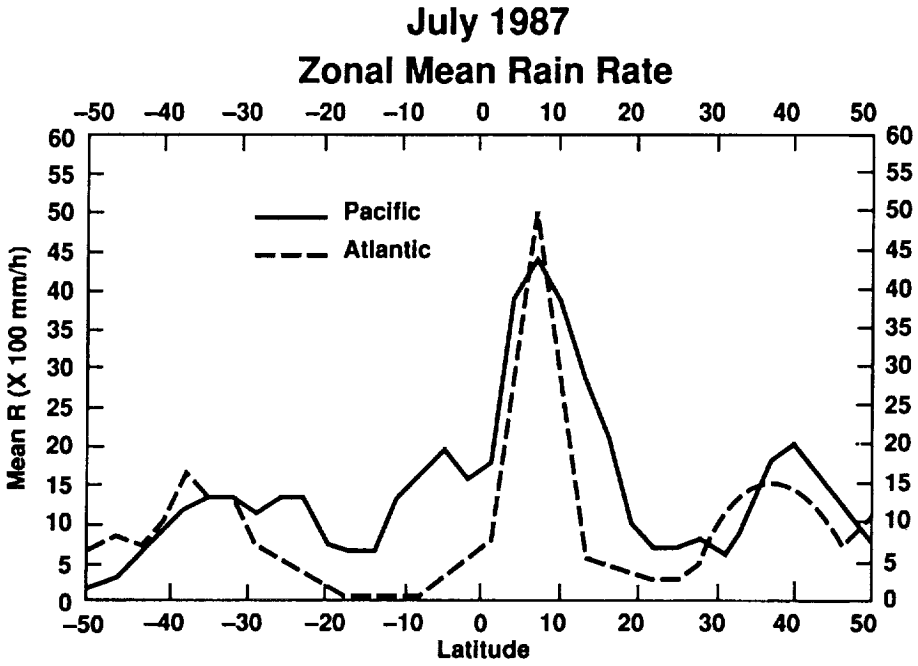

Fig. 11: a) Monthly mean zonally averaged rain rate (mm/h x 100) for the Atlantic and Pacific Oceans derived from SSM/I July 1987 measurements at 19-, 37-, and 85- GHz.

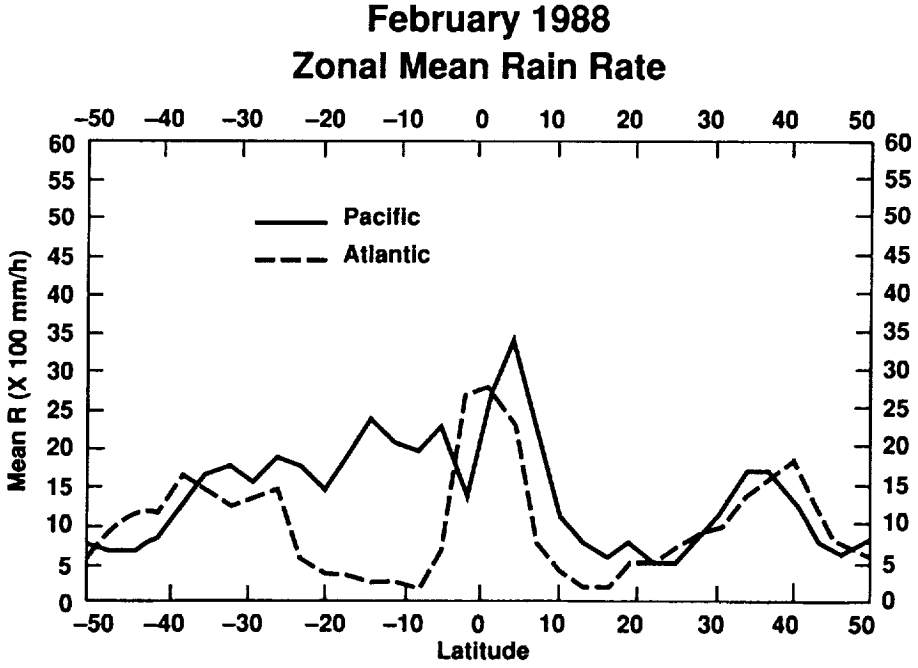

b) Monthly mean zonally averaged rain rate (mm/h x 100) for the Atlantic and Pacific Oceans derived from SSM/I Feb. 1988 measurements at 19-, 37-, and 85- GHz.

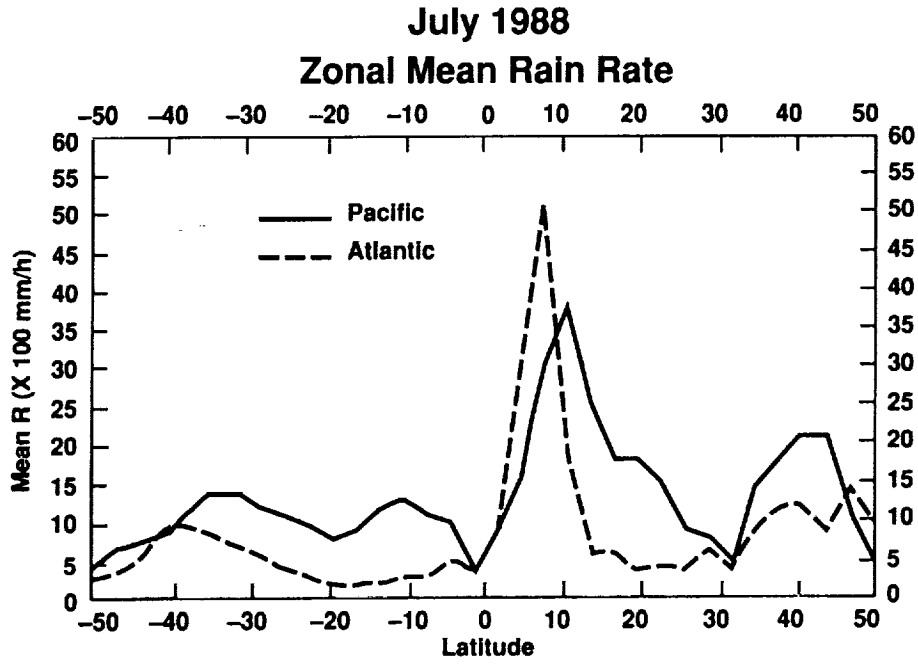

c) Monthly mean zonally averaged rain rate (mm/h x 100) for the Atlantic and Pacific Oceans derived from SSM/I July 1988 measurements at 19-, 37-, and 85- GHz.

Discussion and Conclusion

The rain rate retrieval algorithm developed here constitutes an improvement over that of PDNSL. Two additional independent pieces of information that are elicited from SSM/I data enable us to discriminate primarily the stratiform rain from the convective rain.

The empiricism that is inherent in the development of the retrieval method, i.e., eq. (2), is necessitated because of the complex interplay between the convective phenomena that are evolving in space and time over the global oceans on one hand and the microwave radiative transfer on the other. These two processes are physically independent. One may assume the interaction of these two processes can be simulated with a computer. This will require elaborate numerical schemes, with a considerable number of independent variables, to produce the brightness temperature observed by the satellite radiometers. Ground-truth verification will finally validate such a procedure.

To simplify this problem, in this study we have assumed based on rain gauge data that the complex convective dynamics produce in a given rain scene a log-normal rain rate distribution in space. This spatial distribution of rain should lead to the spatial distribution of the satellite radiometer-measured brightness temperatures. In this manner, we demonstrate empirically that at 37 GHz, it is not the basic principles of radiative transfer that take precedence but the convective dynamics in explaining the relationship between the *fov*-averaged rain rate and brightness temperatures. Radar backscatter observations support the empirical method developed here. We are not contending, however, that the method we have developed is unique. Since the problem is highly non-linear involving several variables and the information available to us is limited, it is quite possible to alter and/or to improve the method by adding more information obtained from measurements.

References

Adler, R. F., H.-Y. Yeh, N. Prasad, W.-K. Tao, and J. Simpson, 1991. Microwave Simulations of a Tropical Rainfall System with a Three-Dimensional Cloud Model. *J. Appl. Meteor.*, vol. 31, pp. 924-953.

Atlas, D., D. Rosenfeld, and D. B. Wolff, 1990. Climatologically Tuned Reflectivity-Rain Rate Relations and Links to Area-Time Integrals. *J. Appl. Meteor.*, vol. 29, pp. 1120-1135.

Dorman, C. E. and R. H. Bourke, 1979. Precipitation over the Pacific Ocean, 30° S to 60° N. *Mon. Wea. Rev.*, vol. 107, pp. 896-910.

Dorman, C. E. and R. H. Bourke, 1981. Precipitation over the Atlantic Ocean, 30 °S to 70 °N. *Mon. Wea. Rev.*, vol. 109, pp. 554-563.

Feigelson, 1978. Preliminary Radiation Model of a Cloudy Atmosphere, 1, Structure of Clouds and Solar Radiation. *Beitr. Phys. Atmos.*, vol. 51, pp. 203-229.

Gloersen, P. and L. Hardis, 1978. Scanning Multichannel Microwave Radiometer (SMMR) Experiment. *Nimbus 7 User's Guide*. Edited by C.R. Madris. NASA/GSFC, Greenbelt, MD, pp. 213-245.

Hollinger, J., R. C. Lo, G. Poe, R. Savage, and J. Pierce, 1987. *Special Sensor Microwave/Imager User's Guide*. Naval Research Laboratory, Washington, D.C., 120 pp.

Kummerow, C., R. A. Mack, and I. M. Hakkarinen, 1989. A Self-consistency Approach to Improve Microwave Rainfall Estimation from Space. *J. Appl. Meteor.*, vol. 28, pp. 869-884.

Olson, W. S., 1987. Estimation of Rainfall Rates in Tropical Cyclones by Passive Microwave Radiometry. Ph.D. Thesis. University of Wisconsin. Madison, WI. pp. 292.

Petty, G. W. and K.B. Katsaros, 1990. Precipitation Observed over South China Sea by the Nimbus 7 Scanning Multichannel Microwave Radiometer During Winter MONEX. *J. Appl. Meteor.*, vol. 29, pp. 273-287.

Prabhakara, C., G. Dalu, G. L. Liberti, J. J. Nucciarone and R. Suhasini, 1992. Rainfall Over Oceans: Remore Sensing from Satellite Microwave Radiometers. *Meteor. and Atmos. Phys.*, vol. 47, pp. 177-199.

Prabhakara, C., G. Dalu, R. C. Lo, and N. R. Nath, 1977. Remote Sensing of Seasonal Distribution of Precipitable Water Vapor Over the Oceans and the Inference of Boundary-Layer Structure. *Mon. Wea. Rev.*, vol. 107, pp. 1388-1401.

Prabhakara, C., D. A. Short, W. Wiscsombe, R. A. Fraser, and B. E. Vollmer, 1986. Rainfall Over Oceans Inferred From Nimbus 7 SMMR: Application to 1982-83 El Niño. *J. Climate Appl. Meteor.*, vol. 25, pp. 1464-1474.

Prabhakara, C., I. Wang, A. T C. Chang, and P. Gloersen, 1983. A Statistical Examination of Nimbus 7 SMMR Data and Remote Sensing of Sea Surface Temperature, Liquid Water Content in the Atmosphere and Surface Wind Speed. *J. Climate Appl. Meteor.*, vol. 22, pp. 2023-2037.

Shin, K.-S., P. E. Riba, and G. R. North, 1990. Estimation of Area Averaged Rainfall over Tropical Oceans from Microwave Radiometry: A Single Channel Approach. *J. Appl. Meteor.*, vol. 10, pp. 1031-1042.

Simpson, J., 1988. Tropical Rainfall Measurement Mission (TRMM): Report of the Science Steering Group. NASA/GSFC, Greenbelt, MD. pp. 94.

Smith, E. A. and A. Mugnai, 1992. Foundations for Statistical-Physical Precipitation Retrieval from Passive Microwave Satellite Measurements. Part I: Brightness Temperature Properties of a Time-dependent Cloud Radiation Model. *J. Appl. Meteor.*, vol. 31, pp. 532-552.

Spencer, R. W., H. M. Goodman, and R. E. Hood, 1989. Precipitation Retrieval over Land and Ocean with the SSM/I, Part I: Identification and Characteristics of the Scattering Signal. *J. Atmos. Oceanic Tech.*, vol. 6, pp. 254-273.

Tao, W.-K., J. Simpson, and S.-T. Soong, 1991. Numerical SImulation of a Subtropical Squall Line over Taiwan Strait. *Mon. Wea. Rev.*, vol 119, pp. 2698-2723.

Wilheit, T. T., , 1978. A Review of Microwave Radiometry to Oceanography. *Bound. Layer Meteor.*, vol 13, pp. 277-293.

Wilheit, T. T., J. L. King, E. B. Rodgers, R. A. Nieman, B. M. Krupp, A. S. Milman, J. S. Stratigos, and H. Siddalingsish, 1982. Microwave Radiometric Observations near 19.35, 92, and 183 GHz of Precipitation in Tropical Storm Cora. *J. Appl. Meteor.*, vol 21, pp. 1137-1145.

Wilheit, T. T., A. T. C. Chang, and L. S. Chiu, 1991. Retrieval of Monthly Rainfall Indices from Microwave Radiometric Measurements Using Probability Distribution Functions. *J. Atmos. Oceanic Tech.*, vol. 8, pp. 118-136.

Wu, R. and J. A. Weinman, 1984. Microwave Radiances from Precipitating Clouds Containing Aspherical Ice, Combined Phase, and Liquid Hydrometeors. *J. Geophys. Res.*, vol. 89, pp. 7170-7178.

REPORT DOCUMENTATION PAGE

Form Approved
OMB No. 0704-0188

1. AGENCY USE ONLY *(Leave blank)*	2. REPORT DATE	3. REPORT TYPE AND DATES COVERED
	June 1993	Technical Memorandum

4. TITLE AND SUBTITLE

Convective and Stratiform Rain: Multichannel Microwave Sensing Over Oceans

5. FUNDING NUMBERS

913

6. AUTHOR(S)

C. Prabhakara, J. J. Nucciarone, and G. Dalu

7. PERFORMING ORGANIZATION NAME(S) AND ADDRESS(ES)

Goddard Space Flight Center
Greenbelt, Maryland 20771

8. PERFORMING ORGANIZATION REPORT NUMBER

93B00084

9. SPONSORING/MONITORING AGENCY NAME(S) AND ADDRESS(ES)

National Aeronautics and Space Administration
Washington, D.C. 20546–0001

10. SPONSORING/MONITORING AGENCY REPORT NUMBER

TM–104586

11. SUPPLEMENTARY NOTES

J. J. Nucciarone: Hughes STX Corporation, Lanham, MD; G. Dalu: C.N.R., Area Della Receria Di Cagliari, Italy.

12a. DISTRIBUTION/AVAILABILITY STATEMENT

Unclassified–Unlimited
Subject Category 47
Report is available from the National Technical Information Service, U.S. Dept. of Commerce, 5285 Port Royal Road, Springfield, VA 22151; (703) 557–4650.

12b. DISTRIBUTION CODE

13. ABSTRACT *(Maximum 200 words)*

Measurements made by the Special Sensor Microwave/Imager (SSM/I) radiometer over the oceans, at 19, 37, and 85 GHz in dual polarization, are used to develop a model to classify rain into light-stratiform, moderately convective, and heavy convective types in the mesoscale convective systems (MCS). It is observed that the bulk of the 19- and 37-GHz data are linearly correlated with respect to one another, and generally increase together in brightness as the mean rain rate in the field of view (fov) of the radiometer increases. However, a significant fraction of the data from these channels departs from this linear relationship, reflecting the non-uniform rain that is convective vs. the relatively light stratiform rain. It is inferred from the SSM/I data, in a MCS, when the slope dT_{37}/dT_{19} is greater than unity there are optically thin clouds which produce light uniform rain. On the other hand, when dT_{37}/dT_{19} is close to unity the rain cells have an open structure and correspond to the convective type of rain. The openings between the cells are apparently a result of the downdrafts and/or entrainment. Relatively low values of 85-GHz brightness temperatures that are present when dT_{37}/dT_{19} is close to unity support these views and, in addition, leads us to conclude that when the convection is heavy this brightness temperature decreases due to scattering by hydrometeors. On the basis of this explanation of the SSM/I data, an empirical rain retrieval algorithm is developed. Radar backscatter observations over the Atlantic Ocean next to Florida are used to demonstrate the applicability of this method. Three monthly mean maps of rainfall over the oceans, from 50° N to 50° S, are presented to illustrate the ability of this method to sense seasonal and interannual variations of rain.

14. SUBJECT TERMS

Convective–Stratiform Rain, Microwave Remote Sensing, Satellite Radiometry

15. NUMBER OF PAGES

41

16. PRICE CODE

17. SECURITY CLASSIFICATION OF REPORT	18. SECURITY CLASSIFICATION OF THIS PAGE	19. SECURITY CLASSIFICATION OF ABSTRACT	20. LIMITATION OF ABSTRACT
Unclassified	Unclassified	Unclassified	Unlimited